



**Titre:** Re-evaluating monazite as a record of metamorphic reactions  
Title:

**Auteurs:** Kyle P. Larson, Sudip Shrestha, John M. Cottle, Carl Guilmette, T. Alex Johnson, H. Daniel Gibson, & Félix Gervais  
Authors:

**Date:** 2022

**Type:** Article de revue / Article


**Référence:** Larson, K. P., Shrestha, S., Cottle, J. M., Guilmette, C., Johnson, T. A., Gibson, H. D., & Gervais, F. (2022). Re-evaluating monazite as a record of metamorphic reactions. *Geoscience Frontiers*, 13(2), 101340 (18 pages).  
Citation: <https://doi.org/10.1016/j.gsf.2021.101340>

 **Document en libre accès dans PolyPublie**  
Open Access document in PolyPublie

**URL de PolyPublie:** <https://publications.polymtl.ca/10648/>  
PolyPublie URL:

**Version:** Version officielle de l'éditeur / Published version  
Révisé par les pairs / Refereed

**Conditions d'utilisation:** CC BY-NC-ND  
Terms of Use:

 **Document publié chez l'éditeur officiel**  
Document issued by the official publisher

**Titre de la revue:** *Geoscience Frontiers* (vol. 13, no. 2)  
Journal Title:

**Maison d'édition:** Elsevier  
Publisher:

**URL officiel:** <https://doi.org/10.1016/j.gsf.2021.101340>  
Official URL:

**Mention légale:** ©2021 China University of Geosciences (Beijing) and Peking University. Production and hosting by Elsevier B.V. This is an open access article under the CC BY-NC-ND license (<http://creativecommons.org/licenses/by-nc-nd/4.0/>).  
Legal notice:

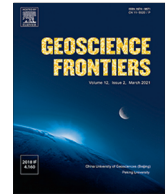
HOSTED BY



ELSEVIER

Contents lists available at ScienceDirect

Geoscience Frontiers

journal homepage: [www.elsevier.com/locate/gsf](http://www.elsevier.com/locate/gsf)

Research Paper

# Re-evaluating monazite as a record of metamorphic reactions

Kyle P. Larson<sup>a,\*</sup>, Sudip Shrestha<sup>b</sup>, John M. Cottle<sup>c</sup>, Carl Guilmette<sup>d</sup>, T. Alex Johnson<sup>c</sup>,  
H. Daniel Gibson<sup>e</sup>, Félix Gervais<sup>f</sup><sup>a</sup> Department of Earth, Environmental and Geographic Sciences, University of British Columbia Okanagan, 3247 University Way, Kelowna, BC V1V 1V7, Canada<sup>b</sup> Fipke Laboratory for Trace Element Research, University of British Columbia Okanagan, 3247 University Way, Kelowna, BC V1V 1V7, Canada<sup>c</sup> Department of Earth Science, University of California, Santa Barbara, Santa Barbara, CA 93106-9630, USA<sup>d</sup> Géologie et Génie Géologique, Université Laval, Québec City, Quebec, Canada<sup>e</sup> Department of Earth Sciences, Simon Fraser University, 8888 University Drive, Burnaby, BC V5A 1S6, Canada<sup>f</sup> Département des Génies Civil, Géologique et des Mines, Polytechnique Montréal, Montréal, QC H3T 1J4, Canada

## ARTICLE INFO

### Article history:

Received 26 June 2021

Revised 18 November 2021

Accepted 2 December 2021

Available online 6 December 2021

Handling Editor: R.M. Palin

### Keywords:

Monazite petrochronology

Phase equilibria modelling

Geochronology

P-T-t paths

## ABSTRACT

This study presents a re-examination of historical specimens (DG136 and DG167) from the Monashee complex in the southeastern Canadian Cordillera that are critical to the current understanding of rare earth element (REE) distribution between garnet and monazite (and other accessory minerals) during metamorphism. Nine-hundred and fifty-one new monazite petrochronology spot analyses on 29 different grains across two specimens outline detailed (re)crystallization histories. Trace element data collected from the same ablated volume, interpreted in the context of new phase equilibria modelling that includes monazite, xenotime and apatite, link ages to specific portions of the pressure–temperature (P-T) paths followed by the specimens. These linkages are further informed by garnet Lu–Hf geochronology and xenotime petrochronology. The clockwise P-T paths indicate prograde metamorphism was ongoing by ca. 80 Ma in both specimens. The structurally deeper specimen, DG136, records peak P-T conditions of ~755–770 °C and 8.8–10.4 kbar, interpreted to coincide with (re-)crystallization of low Y monazite at ~75–70 Ma. Near-rim garnet isopleths from DG167 cross in the observed peak assemblage field at ~680 °C and 9.3 kbar. These conditions are interpreted to correspond with low Y monazite (re-)crystallisation at ~65 Ma. Both specimens record decompression along their retrograde path coincident with high Y 70–55 Ma and 65–55 Ma monazite populations in DG136 and DG167, respectively. These findings broadly agree with those initially reported ~20 years ago and confirm early interpretations using trace elements in monazite as generally reliable markers of metamorphic reactions. Modern phase equilibria modelling and *in situ* petrochronological analysis, however, provide additional insight into monazite behaviour during anatexis and the effects of potential trace element buffering by REE-bearing phases such as apatite.

© 2021 China University of Geosciences (Beijing) and Peking University. Production and hosting by Elsevier B.V. This is an open access article under the CC BY-NC-ND license (<http://creativecommons.org/licenses/by-nc-nd/4.0/>).

## 1. Introduction

Quantifying the geological record of phase reactions in rocks has been paramount in understanding the processes active during metamorphic, tectonic, plutonic, and fluid-related events (e.g. Waters, 2019). In metamorphic rocks, changes in phase and/or mineral chemistries in response to changing conditions (e.g. pressure, temperature, H<sub>2</sub>O saturation, etc.) provide an opportunity to quantify the absolute value of those parameters (e.g. Powell et al., 1998). This is facilitated by experimental and theoretical thermo-

dynamic data and models that can be used to back-calculate the conditions of interest when other variables such as mineral and whole rock chemical composition and total volatile content, for example, are known. The field of metamorphic petrology now commonly employs methodologies to integrate mineral textural observations, mineral and bulk rock chemical composition, and thermodynamic datasets and activity models to re-trace the pressure–temperature–composition (P-T-X) histories of rock specimens (e.g. Connolly, 1990). Moreover, recent advances using non-traditional instrumentation, such as Raman Spectroscopy to quantify quartz encapsulation pressure in garnet (Enami et al., 2007) for example, promise to provide even more insight and detailed control on the P-T-X path a metamorphic rock has followed.

\* Corresponding author.

E-mail address: [kyle.larson@ubc.ca](mailto:kyle.larson@ubc.ca) (K.P. Larson).

While P-T-X data are critical for understanding the history of a metamorphic rock, it is important to put them in a temporal context. Quantifying when geological events occurred is required for any assessment of geological rate and duration or non-relative determination of Earth's history. Advancements in geochronology over the past decade now allow near-routine *in situ* investigation of geochronometers such as monazite, zircon and titanite. Moreover, many recent geochronological studies also analyse trace element concentrations from the same ablated material used for isotopic determinations (Kylander-Clark et al., 2013). This influx of petrochronological or "time-stamped" data has allowed researchers to make informed correlations between the geochemistry and age of a chronometer and the metamorphic reactions that occurred within rock specimens.

Some of the early work that linked geochronometer chemistry to bulk-rock reactions included qualitative and quantitative *in situ* and separated monazite chemical investigations paired with isotope dilution thermal ionization mass spectrometry (ID-TIMS), laser ablation multi collector inductively coupled plasma mass spectrometry (LA-MC-ICP-MS) and sensitive high resolution ion mass spectrometry (SHRIMP) geochronology (Foster et al., 2000, 2002, 2004; Gibson et al., 2004; Kohn et al., 2005; McFarlane et al., 2005). This work identified linkages between age and chemical zonation of monazite, particularly in heavy rare earth elements (HREE), commonly generalized through Y content. Previous studies by Foster et al. (2000, 2002, 2004) and Gibson et al. (2004), in particular, have become classic that have informed prevailing thought on how changes in monazite trace element chemistry are linked to chemical reactions. The linking of the HREE + Y budget of monazite to the stability of garnet in metapelites has become commonplace (e.g. Stearns et al., 2013; Garber et al., 2017; Williams et al., 2017; Fumes et al., 2019; Godet et al., 2020). The basic interpretation commonly employed is that garnet controls the HREE + Y budget available in the rock (e.g. Pyle et al., 2001; Spear and Pyle, 2002) and as such, when garnet is growing or is stable, there would be limited HREE available to be taken up by monazite leaving any monazite that formed at that time relatively depleted in HREE + Y. The converse to that is when garnet is breaking down and HREE + Y is liberated into the system, any monazite grown at that time would be relatively enriched in HREE + Y. Further complications arise when the rock undergoes significant anatexis (Kohn et al., 2005; Yakymchuk and Brown, 2014; Johnson et al., 2021) or contain significant amounts of other HREE-bearing phosphates (Larson et al., 2019), however, for most clockwise P-T paths, the HREE budget is still dominated by the modal garnet proportion (Shrestha et al., 2019).

At nearly the same time as the Foster et al. and Gibson et al. works were published, another set of studies that examined trace element partitioning between garnet and chronometer phases were carried out (Hermann and Rubatto, 2003; Buick et al., 2006; Rubatto et al., 2006). This work quantitatively examined the chemistry of accessory mineral chronometers and garnet in metamorphic rocks to derive partitioning coefficients for various elements including, critically for monazite studies, HREE. While these findings have been used by researchers to interpret linkages between metamorphism and geochronology in many studies, subsequent works have demonstrated that partitioning of HREE within monazite may be significantly more complex than previously thought. For example, work on amphibolite facies metapelites with textural and spatial characteristics that indicate monazite and garnet grew together do not appear to reproduce expected partitioning coefficients (Warren et al., 2018; Larson et al., 2019; Shrestha et al., 2019). Moreover, a detailed examination of garnet and monazite trace element partitioning indicates that partitioning is at least partially temperature dependent, especially for HREE (Hacker et al., 2019). These studies demonstrate that our understanding

of HREE incorporation into monazite is incomplete and as such, the simplistic view of HREE + Y budgeting that has been implemented in many recent works should be revisited.

## 2. This study

In order to re-assess the outcomes of some of the most influential studies on HREE partitioning between garnet and monazite, and by extension the myriad works that apply the same basic interpretations derived therein, the present study revisits some of the original specimens examined. Specifically, herein we examine, in detail, specimens DG136 and DG167 (Fig. 1), which were previously investigated in Foster et al. (2002, 2004) and Gibson (1997). In the original studies, much of monazite dated were extracted from crushed material. As such, textural information and original spatial positions of those grains were not preserved. Moreover, while monazite trace elements were quantified in some of the grains examined, it was done so using an electron probe microanalyser (EPMA), which is subject to significant interferences when analysing REE, and was only carried out in select grains. The limited LA-MC-ICP-MS analyses conducted in DG136 and DG167 included rastering the laser beam to ablate material. While rastering was necessary to avoid down-hole element fractionation, it limited the spatial resolution of analyses. Finally, while the outcomes of the studies are commonly cited in terms of allanite, monazite, and garnet interaction, it is noted that the specimens also contain apatite and xenotime, phosphates that can accommodate substantial amounts of Y and REEs and significantly influence the REE budget of the system.

To re-evaluate the specimens examined in previous studies, we use a combined approach of high density *in situ* petrochronological analyses using current Laser Ablation Split Stream (LASS) technologies, LA-ICP-MS garnet trace element mapping, Lu-Hf garnet geochronology and metamorphic phase equilibria modelling including phosphate minerals, to develop detailed P-T-time (t) histories for DG136 and DG167. This integrated, expanded work allows direct assessment of monazite behaviour along the P-T-t path recorded by the specimens and, therefore, re-evaluation of the basic interpretations around Y zoning in monazite that have propagated out from the original, influential studies.

## 3. Methods

The original thin sections of specimens DG136 and DG167 were covered with a glass coverslip; past work was carried out on specimen slabs, which can no longer be located, and mineral separates. Fortunately, the adhesive used for the coverslips was Canadian Balsam, which permitted the removal with the application of gentle heat. This was carried out in the Department of Earth Sciences at the University of Pisa under the direction of Dr. C. Montomoli. Major element compositions of the primary metamorphic phases - garnet, feldspar, biotite and muscovite were obtained using the Cameca SXFiveFE electron microprobe in the Fipke Laboratory for Trace Element Research (FILTER) at the University of British Columbia Okanagan (UBCO). An accelerating voltage of 15 kV, current of 20 nA, spot size of 5  $\mu\text{m}$  and dwell times of 30 s and 15 s on the peak and background, respectively, were used. Analyses were calibrated against reference materials obtained from Micro Analysis Consultants. Results are calculated and reported as atoms per formula unit (a.p.f.u) based on stoichiometric oxygen (220 for mica; 120 for garnet; 80 for feldspar). Garnet end members are reported as almandine [ $\text{Alm} = \text{Fe}^{2+}/(\text{Fe}^{2+} + \text{Mg} + \text{Ca} + \text{Mn})$ ], pyrope [ $\text{Prp} = \text{Mg}/(\text{Fe}^{2+} + \text{Mg} + \text{Ca} + \text{Mn})$ ], grossular [ $\text{Grs} = \text{Ca}/(\text{Fe}^{2+} + \text{Mg} + \text{Ca} + \text{Mn})$ ], and spessartine [ $\text{Sps} = \text{Mn}/(\text{Fe}^{2+} + \text{Mg} + \text{Ca} + \text{Mn})$ ]. Elemental ratios (Mg number in biotite, muscovite and garnet)

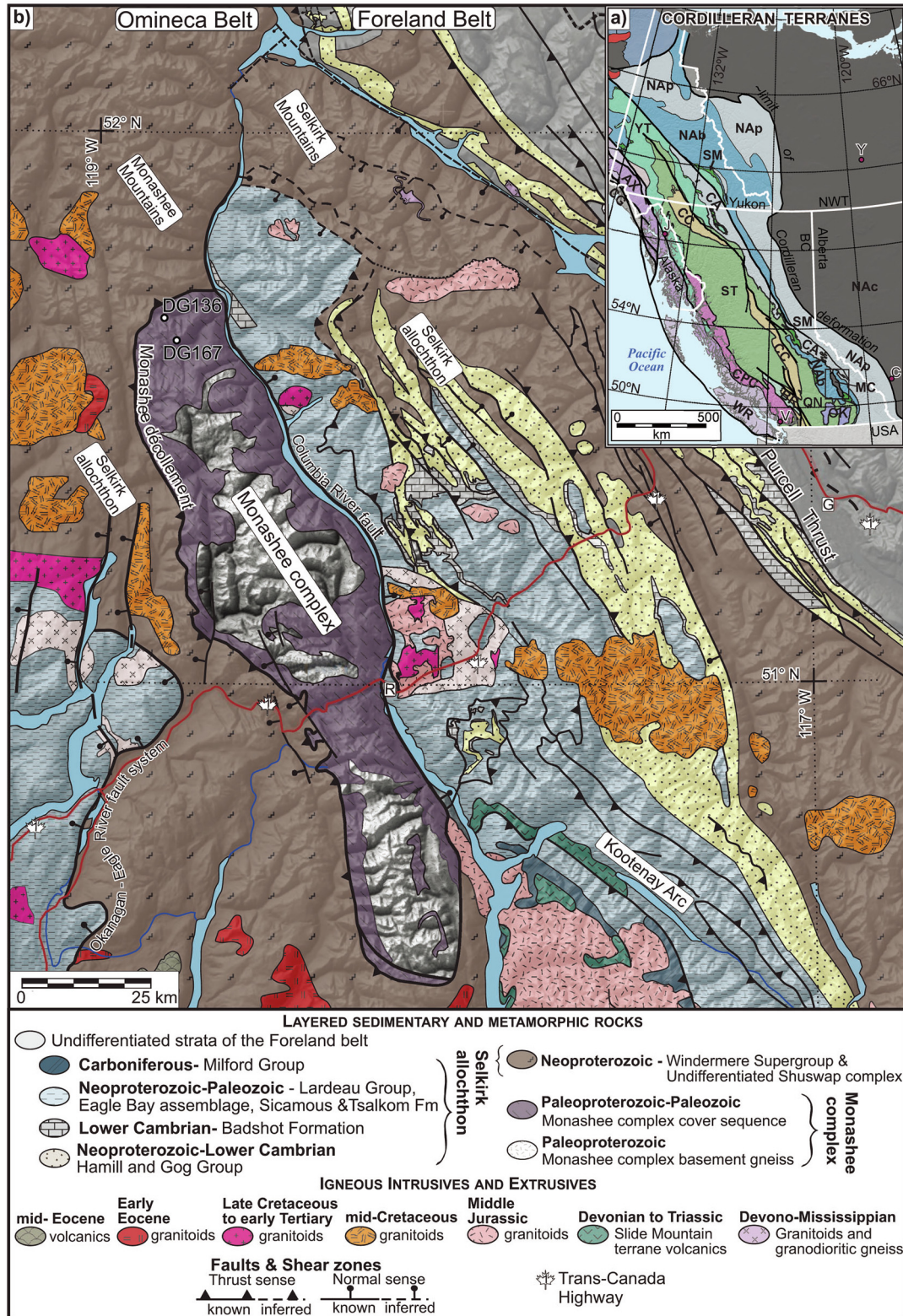


**Fig. 1.** (a) Cordilleran terrane map after Colpron and Nelson (2011). (b) Tectonic assemblage map, southeastern Omineca belt (after Wheeler et al., 1991; Gibson et al., 2008), showing lithologic units of autochthonous Monashee complex (North American basement) and overlying Selkirk allochthon. Towns: C = Calgary; G = Golden; J = Juneau; R = Revelstoke; V = Vancouver; W = Whitehorse; Y = Yellowknife. Terranes: AX = Alexander; BR = Bridge River; CA = Cassiar; CC = Cache Creek; CG = Chugach; CPC = Coast plutonic complex; MC = Monashee complex; Nab = North American basinal; NAc = North American craton & cover; NAP = North American platform; OK = Okanagan; QN = Quesnellia; SM = Slide Mountain; ST = Stikinia; YT = Yukon-Tanana; WR = Wrangellia.

are reported as  $[Mg\# = Mg/(Fe^{2+} + Mg)]$ , whereas plagioclase end-members are reported as anorthite  $[An = Ca/(Na + Ca + K)]$ , albite  $[Ab = Na/(Na + Ca + K)]$  and orthoclase  $[Or = K/(Na + Ca + K)]$ . The full mineral chemistry dataset is available in the [Supplementary Materials](#).

### 3.1. Laser ablation split stream petrochronology

Whole thin sections were mapped using a Cameca SXFiveFE electron microprobe in the FiLTER facility at UBCO for Ti, Y, Na, Ce, P, Ca, Zr, Mg, Fe and K using a 30- $\mu$ m step size with a 30- $\mu$ m diameter beam with a dwell time of 50 ms, an accelerating voltage of 20 kV and a 200 nA current. The Y, Ce, Ca and P maps were used to identify monazite and xenotime targets. This method can locate mineral grains less than 5  $\mu$ m in length. Mineral grain locations are shown *in situ* in the [Supplementary Materials](#). Monazite and xenotime grains were confirmed using an Oxford Instruments X-Max energy dispersive spectrometer on a Tescan Mira 3 XMU scanning electron microscope in the same FiLTER facility.

Quantitative elemental maps of monazite and xenotime grains were made using a Cameca SX-100 electron microprobe at the University of California, Santa Barbara (UCSB). Maps of P, Th, U, Ce, La, Nd, Sm, Pr, Gd, and Y were measured over two analytical passes using a 1  $\mu$ m step size, a fully focused electron beam, and 200 ms dwell time. The accelerating voltage was set at 20 kV and the beam current set at 200 nA. Quantification was done using ZAF matrix and MAN background corrections (Donovan et al., 2016). Data collection and processing was completed using the Probe for EPMA software package. Fully processed maps are provided in the [Supplementary Materials](#).

Monazite and xenotime were analyzed using the LASS system housed at the University of California, Santa Barbara (UCSB) following methods outlined in Kylander-Clark et al. (2013) with modifications as presented in McKinney et al. (2015). Instrumentation consists of a Nu Plasma P3D MC-ICP-MS used to collect U, Th and Pb isotopes, and an Agilent 7700S quadrupole ICP-MS to measure selected trace elements (see petrochronology dataset in the [Supplementary Materials](#)). Both mass spectrometers are connected to a Cetac 193 nm ArF Excimer Laser Ablation system equipped with a HeleX2 ablation chamber. Analyses were carried out using a beam diameter of 8  $\mu$ m, a repetition rate of 3 Hz, a laser fluence of 1.5 J cm<sup>-2</sup>. Minerals were ablated for 15 s, equating to pit depths of  $\sim$ 3  $\mu$ m.

Data reduction, including corrections for baseline, instrumental drift, mass bias, downhole fractionation and age and trace element concentration (using an internal standard approach, assuming stoichiometric P in monazite) calculations, were carried out using Iolite v.2.5 (Paton et al., 2010, 2011).

Utilizing a standard-sample bracketing technique, analyses of reference monazite with known isotopic compositions were measured before and after each set of approximately ten unknown analyses. Isotopic data were normalized to primary reference monazite “44069” ( $424.9 \pm 0.4$  Ma <sup>206</sup>Pb/<sup>238</sup>U ID-TIMS age; Aleinikoff et al., 2006), while Trebilcock was used as secondary reference monazite. Repeat analyses of Trebilcock yielded a <sup>206</sup>Pb/<sup>238</sup>U weighted mean of  $276 \pm 1$  Ma, MSWD = 1.14 (n = 57/61) (c. 273 Ma; Tomascak et al., 1996) and a <sup>208</sup>Pb/<sup>232</sup>Th weighted mean of  $260 \pm 1$  Ma, MSWD = 1.3 (n = 59/61) ( $263.7 \pm 1.0$  Ma; LA ICP-MS age, Kylander-Clark et al., 2013).

Trace element data were normalized to “Bananeira” reference monazite (Kylander-Clark et al., 2013). The long term reproducibility of trace elements using Bananeira at UCSB indicates they are accurate within 5% (2SE – standard error of the mean) (Cottle et al., 2019). All uncertainties are quoted at the 95% confidence or 2SE level and include contributions from the external reproducibility of the primary reference material for the <sup>206</sup>Pb/<sup>238</sup>U

and <sup>208</sup>Pb/<sup>232</sup>Th ratios. The full petrochronology dataset is available in the [Supplementary Materials](#).

Monazite Grain age maps (also available in the [Supplementary Materials](#)) were constructed using the ‘Chrontour’ package (Larson, 2020) for the open R software environment. <sup>208</sup>Pb/<sup>232</sup>Th age and spot location data were interpolated across an extrapolated 500  $\times$  500 grid using the approach of Akima (1978) as implemented in the ‘Akima’ package for the R software environment maintained by A. Gebhardt.

### 3.2. Garnet trace element mapping

Garnet trace element maps were constructed using a Photon Machines 193 nm excimer laser paired with an Agilent 8900 triple quadrupole ICP-MS in the FiLTER facility at UBCO. Raster maps were made using a 80  $\mu$ m diameter laser spot with a 10 Hz rep rate, scanning at 40  $\mu$ m/s. Raw ICP-MS and laser data were integrated and processed using Iolite v.4 (Paton et al., 2011). The software package was also used to extract semi-quantitative trace element concentration profiles across the mineral grains based on assumed stoichiometric (Si) chemistry. Garnet transect chemistry is available in the [Supplementary Materials](#).

### 3.3. Garnet Lu-Hf isotope analysis

Garnet Lu-Hf geochronology was performed at the Washington State University (WSU) Radiogenic Isotope and Geochronology Laboratory. Four handpicked garnet fractions (each between 0.15 g and 0.20 g) and two whole-rock fractions were dissolved and analyzed for their Lu and Hf isotopic compositions. The finely crushed, optically clear garnet fractions were washed with 1 M HCl and rinsed with DI water to remove possible surface contamination prior to dissolution. Following acid digestion, 50- $\mu$ L cuts were removed from each garnet and whole-rock fraction and analyzed for their trace element compositions using an Agilent 7700 quadrupole ICP-MS. Isotopic analysis of the chemically separated Lu and Hf was performed using a Thermo Scientific Neptune Plus MC-ICP-MS at WSU. Procedures for the sample dissolution, spiking, and chemical separation followed those described in Cheng et al. (2008) and Johnson et al. (2018, 2020). Data table is available in the [Supplementary Materials](#).

## 4. Results

### 4.1. Specimen descriptions

The detailed petrography and mineral chemistries of specimens DG136 and DG167 are presented across a series of papers (Gibson et al., 1999; Foster et al., 2002, 2004). The specimens were collected from a late Proterozoic to Paleozoic pelitic schist unit (Scammell and Brown, 1990) within the Monashee complex cover sequence as exposed in the northern part of Frenchman Cap dome (Fig. 1), a metamorphic culmination exposed within the southern Canadian Cordillera of British Columbia, Canada. The rocks were sampled from a transposed anticline-syncline pair in the proximal footwall of the Monashee décollement (Gibson et al., 1999), a major structure that has been postulated as the main thrust-sense detachment for the orogen (Read and Brown, 1981; Brown et al., 1992; Brown and Gibson, 2006; Gervais and Brown, 2011; Simony and Carr, 2011). Specimens DG136 and DG167 were collected from the same stratigraphic horizon in the opposite limbs of an overturned fold  $\sim$ 600 m and  $\sim$ 3000 m below the décollement, respectively (Fig. 1; Gibson et al., 1999). The rocks at these locations coincide with metamorphic zones B and C of Gervais (2018), respectively. Moreover, specimen DG136 was collected

within the same continuously exposed alpine outcrop as specimen FG-465B reported by Gervais and Crowley (2017).

Specimen DG136 is an anatexite-bearing pelitic schist characterized by an assemblage of generally interlocking Qz + Pl + Ky + Bt + Grt + Kfs + Rt ± Sil (Fig. 2A; abbreviations throughout after Whitney and Evans, 2010). Leucosome in the exposure is Grt + Ky bearing (Gervais and Crowley, 2017; Gervais, 2018). Quartz and biotite occur as aligned inclusions in kyanite; smaller randomly oriented quartz inclusions are noted in some garnet grains (Fig. 2A). K-feldspar is rare in the specimen, but where present is associated with biotite, kyanite and plagioclase (Fig. 2A, C). Kyanite in DG136 are commonly surrounded by moats of muscovite (Fig. 2D, E), while much of the biotite appears to have been replaced by a mixture of chlorite, muscovite and a Ti-bearing oxide (Fig. 2B–D). Sillimanite, while not observed in the present study, has been noted in equivalent rocks by Foster et al. (2004) and Gervais (2018).

Specimen DG167 is a pelitic schist characterized by a well-developed planar fabric defined by aligned mica and sillimanite (Fig. 3A). The outcrop from which it was collected belongs to zone C of Gervais (2018), which contains less than 10% leucosome by volume. The specimen has a primary assemblage of Qz + Pl + Ms + Bt + Grt + Ky + Sil. Garnet grains are poikilitic, dominated by inclusions of quartz and biotite (Fig. 3A, B). The same inclusions are found locally within kyanite grains (Fig. 3C). Sillimanite in the thin section occurs as fibrolite, in close association with biotite (Fig. 3D, E). Garnet grains are variably rimmed by quartz, biotite and/or sillimanite (Fig. 3A). Some of the matrix biotite is partially replaced by chlorite (Fig. 3C).

## 4.2. Mineral chemistry

### 4.2.1. Garnet

Garnet in DG136 is dominantly almandine with a composition of Alm<sub>0.70–0.78</sub> Prp<sub>0.09–0.18</sub> Grs<sub>0.05–0.13</sub> Sps<sub>0.01–0.06</sub> and Mg#<sub>0.11–0.21</sub> (Fig. 4). Garnet elemental zoning in DG136 is characterized by decreasing spessartine from core towards rim (Sps<sub>0.05</sub> to Sps<sub>0.01</sub>) with a sharp increase at the outer rim (Sps<sub>0.06</sub>). Excluding material proximal to through-going cracks, zonation in almandine, pyrope and grossular is more variable. Almandine is essentially flat across much of the grain including the inner rim (~Alm<sub>0.71</sub>) and increases across the outer rim (Alm<sub>0.78</sub>). Pyrope increases gradually from just outside the cracked interior of the grain to a maximum (Prp<sub>0.13</sub> to Prp<sub>0.18</sub>) before a sharp decrease at the outer rim (Prp<sub>0.11</sub>). Mg# follows pyrope, generally increasing from 0.15 to 0.20 toward the inner rim before a marked drop to 0.12 across the outer rim. Finally, grossular decreases slightly across the inner rim (Grs<sub>0.13</sub> to Grs<sub>0.12</sub>) before a more pronounced decrease towards and across the outer rim (Grs<sub>0.05</sub>).

Garnet grains in DG167 are also dominantly almandine with composition of Alm<sub>0.63–0.74</sub> Prp<sub>0.10–0.21</sub> Grs<sub>0.05–0.17</sub> Sps<sub>0.01–0.09</sub> and Mg#<sub>0.13–0.24</sub> (Fig. 4). Elemental zoning in garnet is variably preserved and typically truncated at resorbed grain boundaries. Where well-preserved, zonation shows a gradual decrease in grossular and spessartine away from grain cores (Grs<sub>0.17</sub> Sps<sub>0.09</sub> to Grs<sub>0.06</sub> Sps<sub>0.02</sub>) compensated by an increase in almandine and pyrope (Alm<sub>0.63</sub> Prp<sub>0.10</sub> to Alm<sub>0.67</sub> Prp<sub>0.20</sub>). Almandine and spessartine increase at the outer rims (Alm<sub>0.73</sub> Sps<sub>0.07</sub>), while pyrope (Prp<sub>0.14</sub>) decreases and grossular is largely unchanged. Mg# follows the same pattern as that followed by pyrope with the lowest values associated with the grain core (0.14), a plateau of higher values across the mantle and inner rim (0.21) and a decrease across the outer rim (0.16).

The general bell-shaped and inverted bell-shaped elemental zonation noted in the specimens is broadly consistent with that expected during prograde garnet growth in metapelitic rocks

(Woodsworth, 1977). Moreover, the increases in spessartine and almandine (and decrease in pyrope) in the outer rims may indicate partial resorption (Kohn and Spear, 2000).

### 4.2.2. Biotite/muscovite/feldspar

Biotite grains analyzed in both specimens are annitic in composition. Those in specimen DG136 have a narrow compositional range with Mg# between 0.40 and 0.42 and Ti content between 0.41 a.p.f.u. and 0.50 a.p.f.u. with no relationship to textural setting. Finite Gaussian mixture modelling using the program PeakFit (Kerswell et al., 2021) of Ti-in-biotite-derived temperatures (Henry et al., 2005) indicates a single peak at  $\sim 710 \pm 4^\circ\text{C}$ . Muscovite in the same specimen is variable in Si content (6.08–6.24 a.p.f.u.) and Mg# (0.42–0.47), again with no distinct textural trends. Feldspar compositions range across plagioclase (Ab<sub>0.60–0.68</sub> An<sub>0.30–0.33</sub>) and K-feldspar (Or<sub>0.88–0.96</sub>) with no systematic trends.

Biotite in DG167 varies in both Mg# and Ti content. The Mg# ranges between 0.46 and 0.51 while measured Ti content is between 0.13 a.p.f.u. and 0.45 a.p.f.u. While the Mg# of biotite inclusions in garnet overlaps with that in matrix grains, the Ti content in inclusions (0.13–0.17 a.p.f.u.) is significantly lower than the matrix (0.26–0.44 a.p.f.u.). Finite Gaussian mixture modelling using the program PeakFit (Kerswell et al., 2021) of Ti-in-biotite-derived temperatures (Henry et al., 2005) for inclusions and matrix grains outline peaks at  $\sim 510 \pm 5^\circ\text{C}$  and  $680 \pm 2^\circ\text{C}$ , respectively. Much like in DG136, muscovite compositions are variable in DG167 with Si ranging between 5.96 a.p.f.u. and 6.14 a.p.f.u., and Mg# between 0.51 and 0.62 without any correlation with textural setting. Feldspar only occurs as plagioclase (An<sub>0.28–0.36</sub>) with grains included within garnet having anorthite content (An<sub>0.35–0.36</sub>) at the higher end of the near-garnet and matrix grain compositional range.

## 4.3. Phase equilibria modelling

Phase diagrams were built following the procedure of Shrestha et al. (2019) using the modified Holland and Powell (1998 updated 2004) thermodynamic dataset with additional thermodynamic data for phosphates and phosphate melts adapted from Spear and Pyle (2010). All solution models used are as described therein. Phase diagrams were calculated in the MnO-Na<sub>2</sub>O-CaO-K<sub>2</sub>O-FeO-MgO-Al<sub>2</sub>O<sub>3</sub>-SiO<sub>2</sub>-H<sub>2</sub>O-TiO<sub>2</sub>-Fe<sub>2</sub>O<sub>3</sub> + Y<sub>2</sub>O<sub>3</sub>-Ce<sub>2</sub>O<sub>3</sub>-P<sub>2</sub>O<sub>5</sub>-F (MnNCK FeMASHTO + YCePF) system. Calculations, phase diagrams and pixelmap data were generated using the Theriak-Domino program (de Capitani and Brown, 1987; de Capitani and Petrakakis, 2010). Pixelmap datasets were processed using the open, freely available PixelMapR script (Larson and Ambrose, 2021) to generate phase mode and isopleth diagrams. Whole rock compositions used for modelling are as published in Foster et al. (2002) with mineral compositions as noted above with one exception. The garnet grains in the thin section of DG136 are not well preserved. They are cracked, with evidence of alteration of elemental zoning along those cracks, and incomplete, cut off by the edge of the section. Because of this, we choose to use the garnet transect data presented in Foster et al. (2004) across a well-faceted, apparently complete garnet grain to inform our phase equilibria models. Two different phase models were calculated for each specimen: (i) excess water and (ii) sufficient water to saturate the solidus (1 mol.% free H<sub>2</sub>O; DG136 = 4.56 mol.% H<sub>2</sub>O, DG167 = 5.44 mol.% H<sub>2</sub>O) along the inferred pressure-temperature path. An additional model (2.45 mol.% H<sub>2</sub>O) was also calculated for DG136 in which the water content was calculated from mineral phase abundances and chemistries following White et al. (2007).

In the following section, we only consider rock-forming and minor phases when evaluating equilibrium P-T conditions, purposefully ignoring monazite. We do this because including phos-

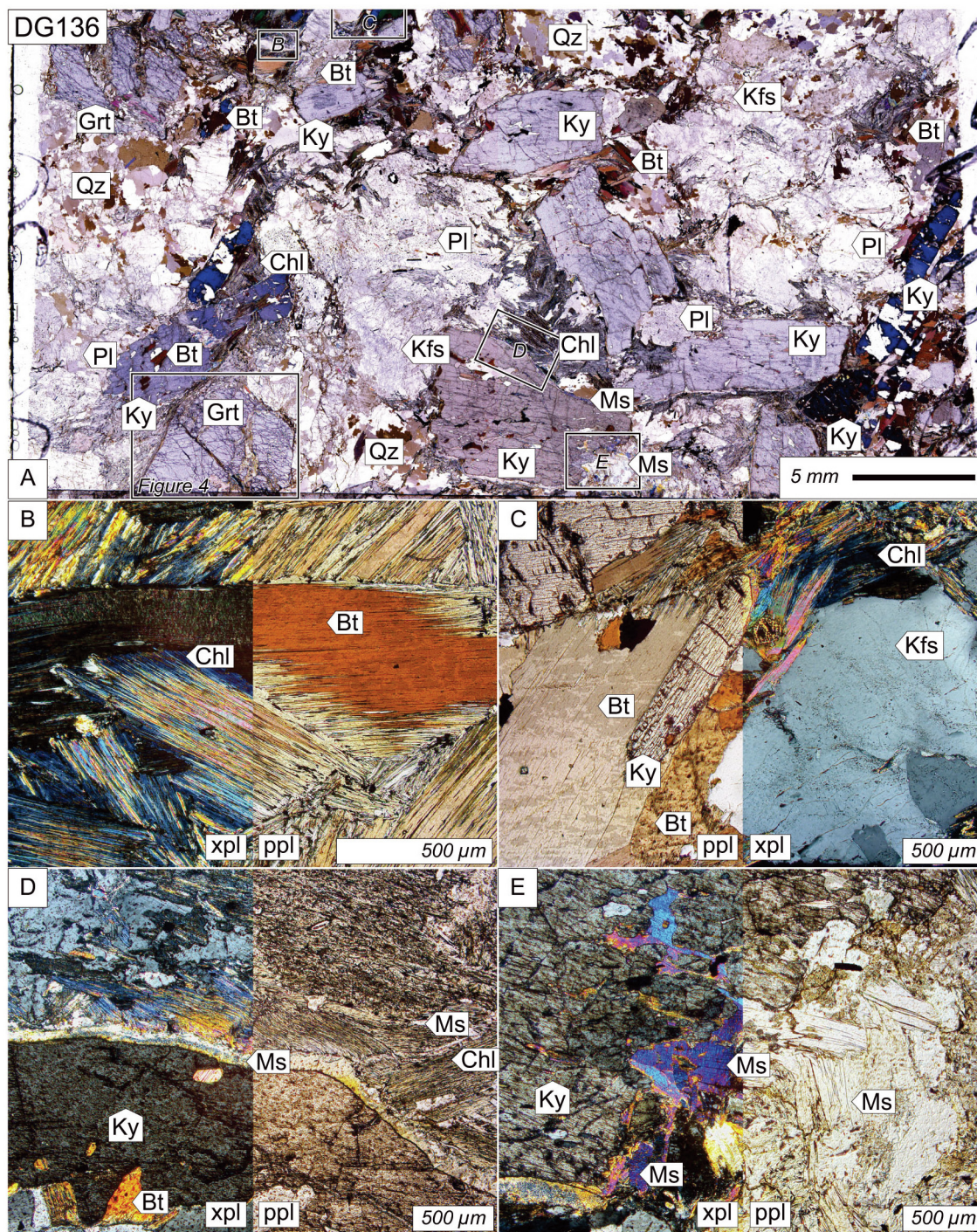


**Fig. 2.** (A) A false colour plane-polarized light photomicrograph of the thin section of DG136 captured with a Russell-Head Instruments G60+ fabric analyser. Locations of photomicrographs shown in B, C, D, E, and the garnet grain investigated in Fig. 4, are shown. (B–E) Cross-polarized and plane-polarized photomicrographs highlighting various textures exhibited in specimen DG136. See text for discussion. Abbreviations are after Whitney and Evans (2010).

phases into phase equilibria models requires additional assumptions (e.g. the relative amounts of F vs. Cl apatite) and the use of non-empirical thermodynamic components (see Spear and Pyle, 2010; Shrestha et al., 2019). Moreover, the modelled behaviour of monazite above the solidus relative to observations is one of the aspects tested in the present work (see below).

#### 4.3.1. DG136

Fig. 5 presents a composite P-T phase diagram for this sample calculated with H<sub>2</sub>O in excess below the solidus (averaged to

650 °C) and enough water to saturate the solidus at higher T. The inferred Qz + Pl + Ky + Bt + Grt + Kfs + melt peak equilibrium assemblage is reproduced as a narrow supra-solidus field of ~750–770 °C and 8.8–10.4 kbar. This field (field 19 in Fig. 5) is bound at the high T end by the disappearance of biotite, at the low T end by the terminal muscovite dehydration melting reaction and the appearance of Kfs, and at lower P by the Ky-Sil transition (sillimanite is noted as a retrograde phase in Gervais and Crowley, 2017). Because Fe<sup>3+</sup>/Fe<sup>Tot</sup> is not rigorously constrained we do not rely on Ti-bearing phase changes.

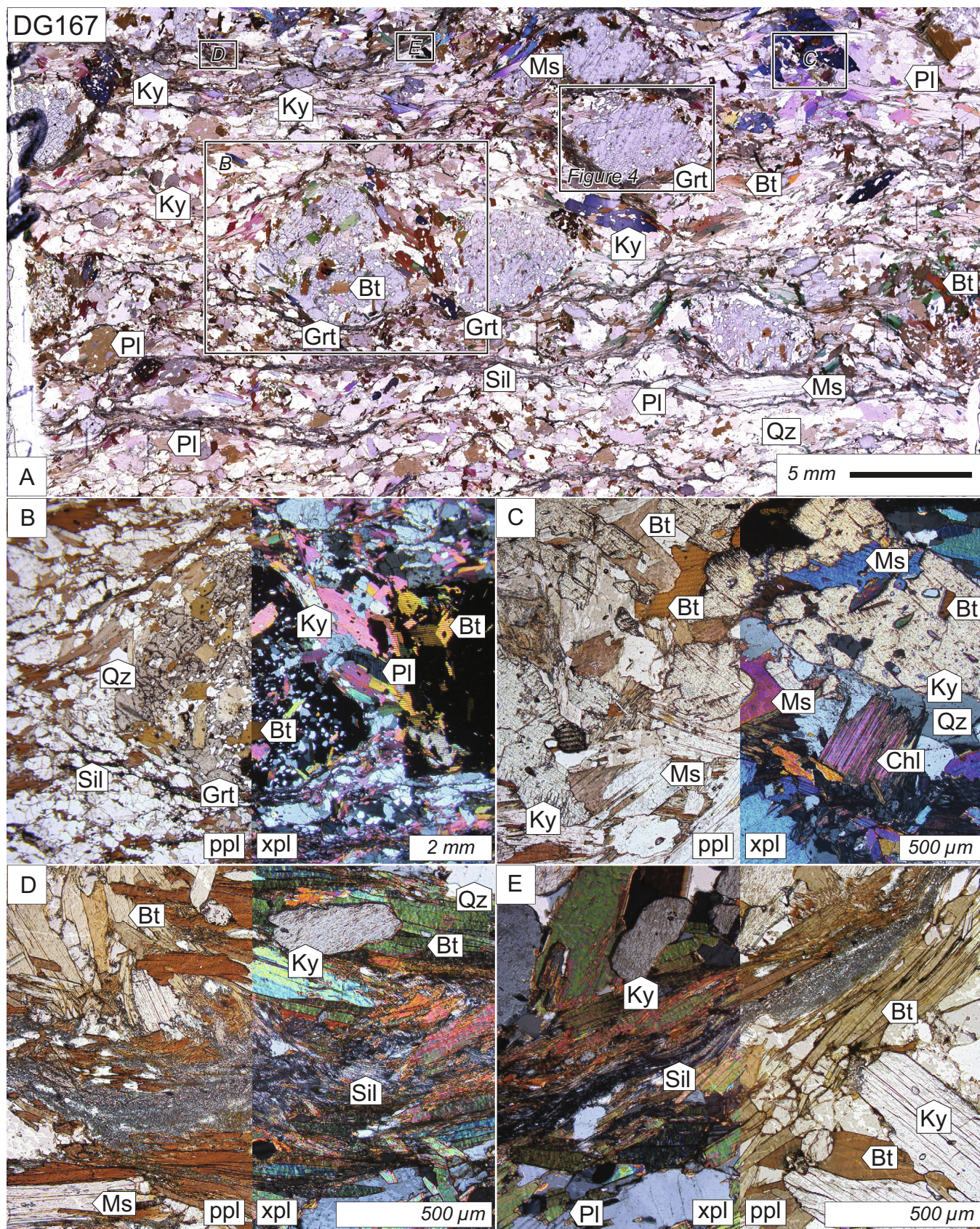


**Fig. 3.** (A) A false colour plane-polarized light photomicrograph of the thin section of DG167 captured with a Russell-Head Instruments G60+ fabric analyser. Locations of photomicrographs shown in B, C, D, E, and the garnet grain investigated in Fig. 4, are shown. (B–E) Cross-polarized and plane-polarized photomicrographs highlighting various textures exhibited in specimen DG167. See text for discussion. Abbreviations are after Whitney and Evans (2010).



Garnet core grossular ( $X_{\text{Grs}} = 0.14$ ) and Mg# (0.15) isopleths from DG136 intersect in a biotite absent staurolite-chlorite-muscovite field below the solidus at a temperature of  $\sim 590$  °C and pressure of  $\sim 7.1$  kbar (Fig. 5). These conditions are significantly higher than the predicted garnet-in boundary, consistent with near-peak intracrystalline diffusion, some degree of overstepping or not analysing equatorial section. We did not observe any biotite inclusions in garnet cores, consistent with the prediction that garnet nucleated and grew in biotite-absent fields. The same isopleths from garnet inner rims ( $X_{\text{Grs}} = 0.06$ , Mg# = 0.2) cross near 8.4 kbar and 710 °C (Fig. 5) in a muscovite-bearing and K-feldspar absent field that does not correspond to the inferred peak assemblage. Late Fe-Mg diffusion at the garnet rim may be partially responsible for this discrepancy. The P-T path is inferred to continue to higher metamorphic conditions to enable the breakdown of muscovite to grow kyanite and K-feldspar in melt followed by biotite breakdown to grow garnet in melt (Gervais and Crowley, 2017).

The return path defines a clockwise loop involving decompression and cooling from peak conditions to between 5 kbar and 6.8 kbar, and  $\sim 690$  °C. The path back across the solidus is informed by the lack of any cordierite record in the system and the rare occurrence of sillimanite (Foster et al., 2004). The rare occurrence of sillimanite is consistent with a path that follows limited changes in the modal proportion of aluminosilicate (see Supplementary Materials). The return path indicated is also consistent with the ubiquitous textural association of biotite and monazite in the matrix (see petrochronology section), as both phases are predicted to grow as the specimen crosses back across the solidus.

The garnet inner rim isopleth intersections outline estimated conditions of prograde garnet growth and minimum peak P-T overlap with those reported in Foster et al. (2004), but are lower than those interpreted in Gervais and Crowley (2017) for a nearby sample. The apparent differences likely reflect a number of compounding factors including the use of different mineral chemistries and solution models in the phase equilibria models (Gervais and Trapy, 2021). The same basic path P-T path, however, including significant decompression and crossing the same major reactions outlined by Gervais and Crowley (2017), is replicated herein.

#### 4.3.2. DG167

Fig. 6 presents a composite P-T phase diagram for this sample calculated with H<sub>2</sub>O in excess below the solidus (averaged to 650 °C) and enough water to saturate the solidus at higher T. The inferred Qz + Pl + Ms + Bt + Grt + Ky peak equilibrium assemblage is reproduced as a large supra-solidus field between  $\sim 670$  °C and  $>750$  °C, and 8.1 kbar to  $>12$  kbar bound at the high T end by the appearance of K-feldspar (not shown in Fig. 6). The low T end of this field is bound by the water-saturated solidus while the low P limit is informed by disappearance of muscovite. We do not consider Ti-phase transitions to inform the P and T of equilibrium, given the limited control on  $\text{Fe}^{3+}/\text{Fe}^{\text{Tot}}$ .

Garnet core isopleths (Mg# = 0.16 and  $X_{\text{Grs}} = 0.17$ ; Fig. 4) intersect near 590 °C and  $\sim 7.5$  kbar in a small chlorite and clinoamphibole-bearing subsolidus field (Fig. 6). These conditions are significantly higher than both the predicted garnet-in boundary and the estimated Ti-in-biotite garnet inclusion temperatures, consistent with some degree of near-peak intracrystalline diffusion, overstepping, or perhaps that the actual core was not analysed. The field is biotite-bearing, consistent with the numerous biotite inclusions across garnet cores. Garnet inner rim values of the same isopleths (Mg# = 0.23 and  $X_{\text{Grs}} = 0.09$ ) cross at higher temperature and pressure, in the field of the observed assemblage just above the solidus at a temperature of  $\sim 680$  °C and a pressure of 9.3 kbar. The predicted melt fraction in the rock is very low, consistent with the absence of melt-related microtextures in the thin sections and

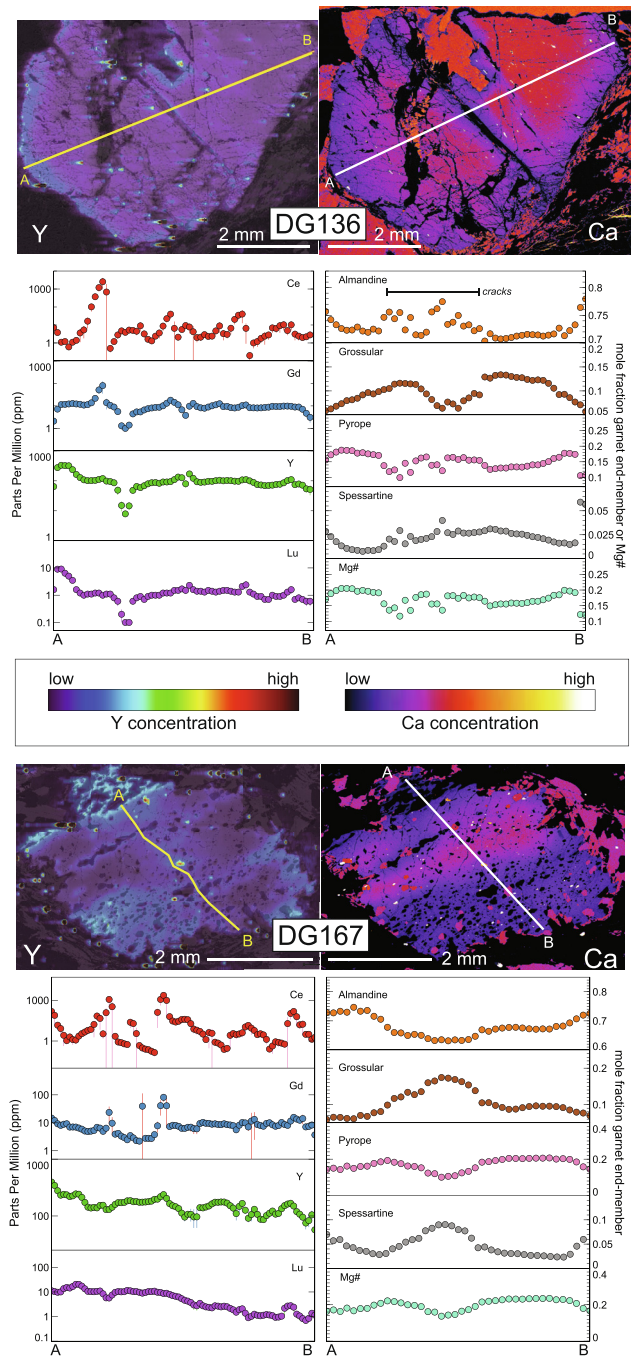


**Fig. 4.** Elemental maps (Y and Ca) of, and transects (trace elements and major elements) across, garnet grains in the two specimens examined. Vertical lines in the trace element transects indicate the uncertainty of the measurements. The locations of the grains examined are depicted in Figs. 2 and 3 for DG136 and DG167, respectively.

with very low proportions of leucosome reported at the outcrop-scale (Gervais, 2018).

The return path is interpreted to follow a clockwise path similar to that noted in DG136 with a significant difference insofar as sillimanite is common in DG167 and associated with the well-developed foliation that wraps around garnet grains. The return path, therefore, must favour sillimanite stability (see Supplemen-

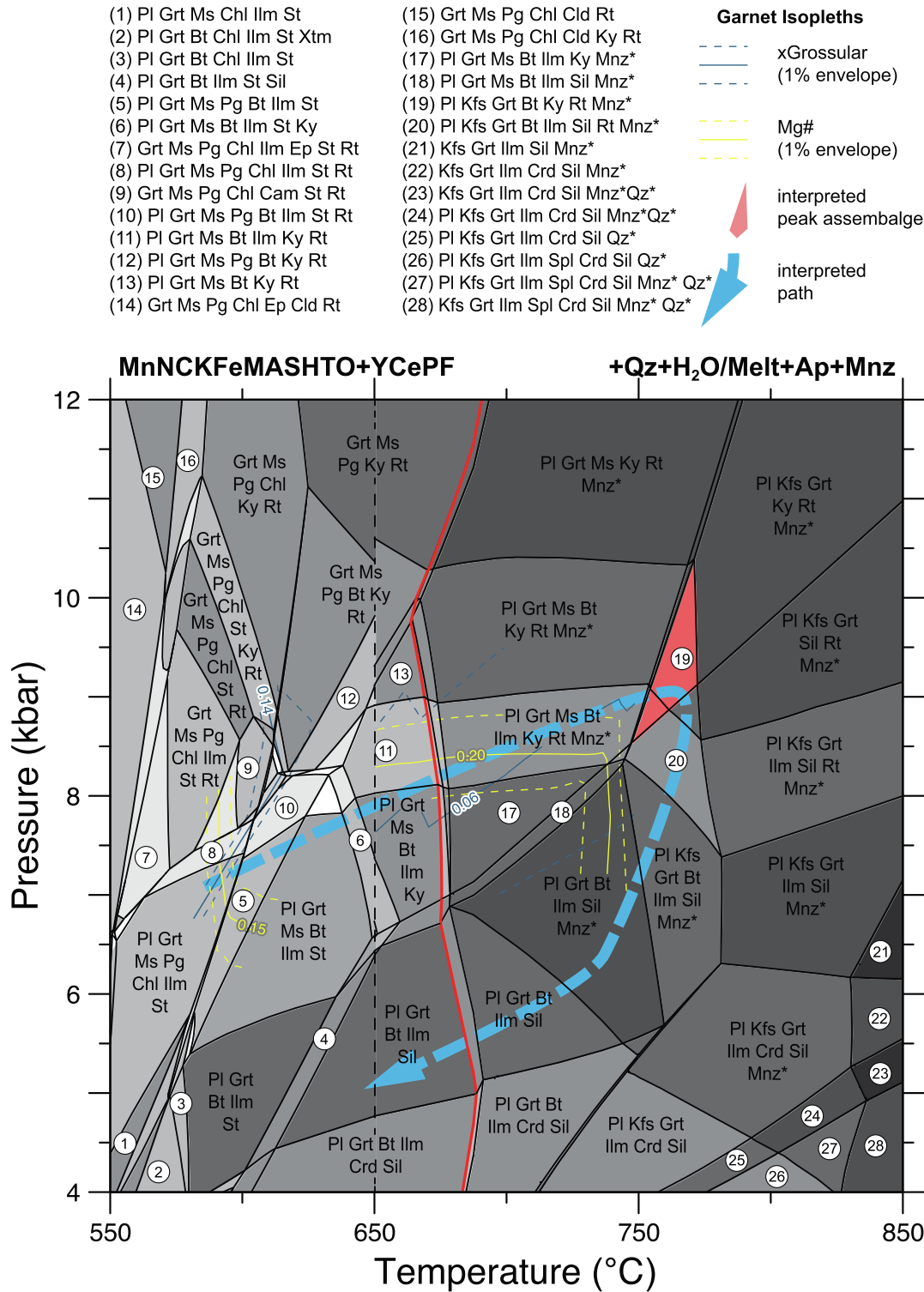


**Fig. 5.** Phase equilibria model for DG136 constructed using Theriak-Domino (after de Capitani and Brown, 1987; de Capitani and Petrakakis, 2010). Isoleths, field of interpreted peak assemblage and inferred pressure-temperature path are as marked. Shading of assemblage fields indicates variance with darker fields corresponding to a higher variance. Red line indicates the solidus; \* indicates the absence of a particular phase. Black dashed line indicates a change in the water content used to calculate the model; excess water at lower temperature and enough water to saturate the solidus at higher temperature. See text for discussion.

tary Materials), though overall decompression as part of the retrograde path is limited by the lack of evidence of cordierite in the specimen. The sillimanite may have derived from the subsolidus reaction:  $Grt + Ms = Sil + Bt$ , which requires decompression below the muscovite-dehydration reaction.

The P-T conditions outlined above are consistent with those previously proposed by Foster et al (2004). In that work, garnet cores are interpreted to have equilibrated at  $559 \pm 10$  °C and  $6.9 \pm 0.3$  kbar while peak conditions reflect a P-T of  $665 \pm 23$  °C and  $8.8 \pm 1.1$  kbar.

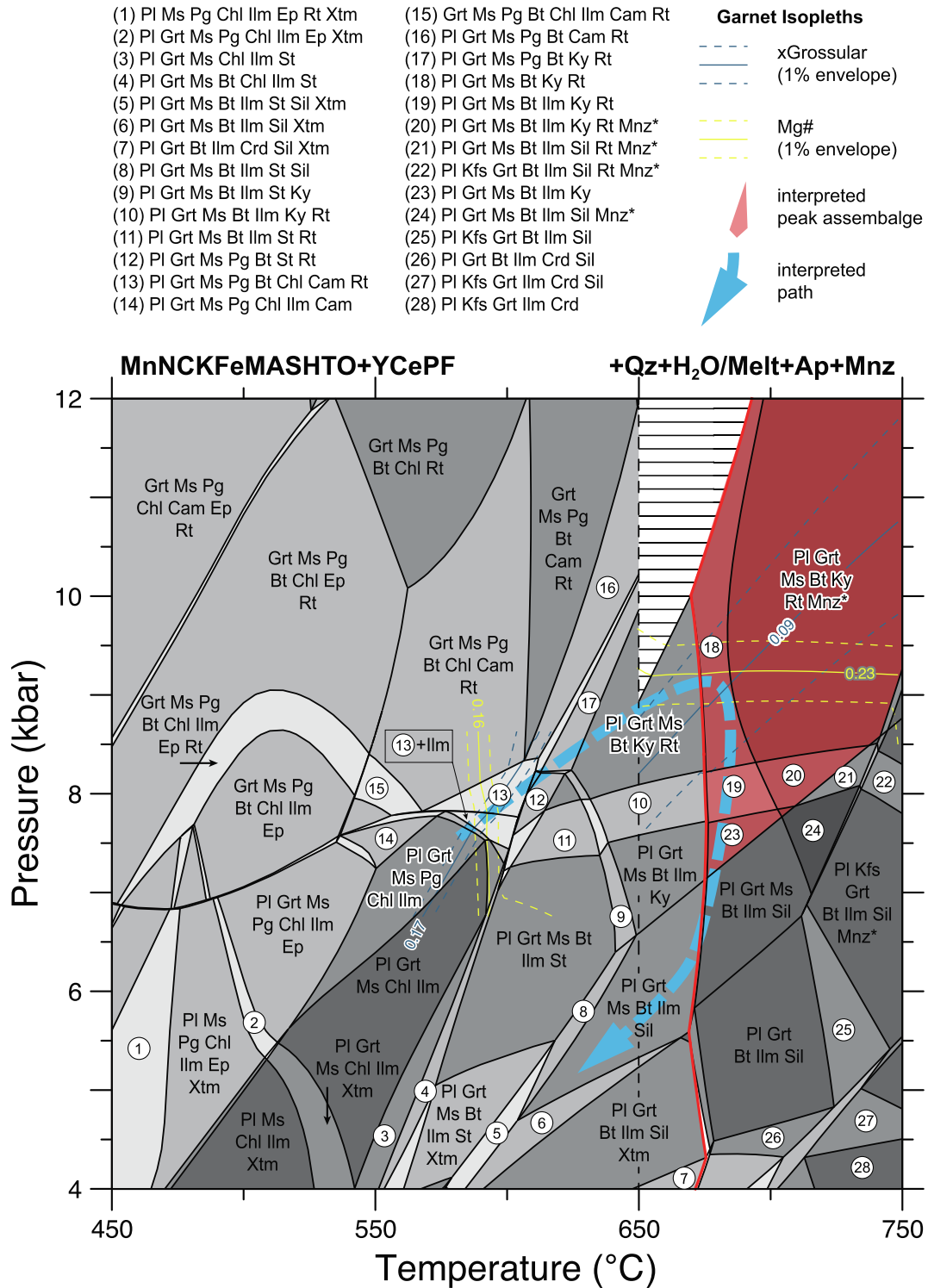


**Fig. 6.** Phase equilibria model for DG167 constructed using Theriak-Domino (after de Capitani and Brown, 1987; de Capitani and Petrakakis, 2010). Isoleths, field of interpreted peak assemblage and inferred pressure temperature path are as marked. Shading of assemblage fields indicates variance with darker fields corresponding with a higher variance. Red line indicates the solidus; \* indicates the absence of a particular phase. Black dashed line indicates a change in the water content used to calculate the model; excess water at lower temperature and enough water to saturate the solidus at higher temperature. The white field with horizontal thin black lines is not included in the model because of incompatibilities between the different water contents used for the models on either side of the 650 °C line. See text for discussion.

#### 4.4. Monazite petrochronology

Monazite analysed in DG136 occurs exclusively in the matrix typically in association with biotite, but locally also sharing grain boundaries with quartz, kyanite and feldspar (see monazite loca-

tions in [Supplementary Materials](#)). The entire exposed surfaces of all 7 grains located in thin section were investigated with 548 laser spots (see grain age maps in the [Supplementary Materials](#)). These analyses yielded  $^{208}\text{Pb}/^{232}\text{Th}$  dates that range from  $113 \pm 4$  Ma to  $52.4 \pm 1.2$  Ma (Fig. 7). There is potential that some of these dates

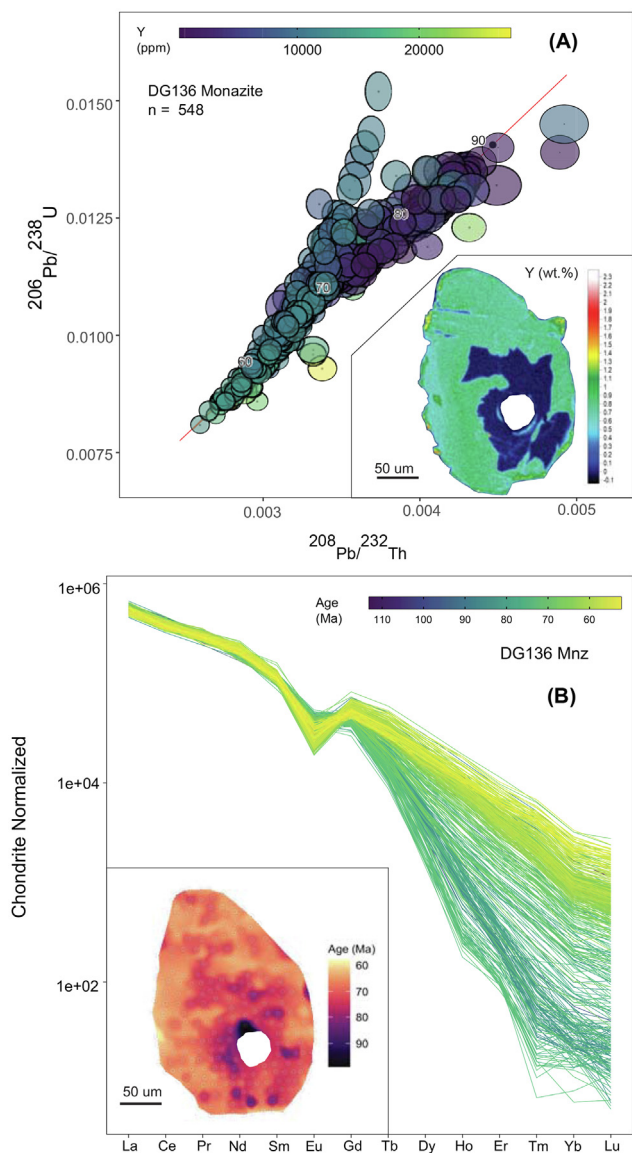


**Fig. 7.** (A)  $^{208}\text{Pb}/^{232}\text{Th}$  versus  $^{206}\text{Pb}/^{238}\text{U}$  concordia plot of monazite geochronological data collected in DG136. Ellipses are coloured by Y content. Inset is an example Y map of a monazite grain from the specimen. (B) Chondrite normalized trace element plot of monazite analyses from DG136 coloured by  $^{208}\text{Pb}/^{232}\text{Th}$  age. Chondrite values are from McDonough and Sun (1995). Inset shows an age map of the same grain shown in the Y map above. All plots were created with the ChronouR package (after Larson, 2020) for the R environment.

represent mixed ages, however, the sheer number of spots analysed and the size of chemical domains relative to the laser spot limit possible mixing issues. A kernel density estimation (KDE) plot of the data outlines a broad main peak at ~65 Ma and a smaller peak at ~85 Ma (Fig. 8). The ~85 Ma monazite generally have moderate Y concentrations (1000–30,000 ppm; Fig. 9A) though a few outliers have higher Y. The data appear to split into two broad populations with younger ages. One population (~75–70 Ma) is associated with low Y concentrations (~200–800 ppm) while the other (~70–55 Ma) is associated with higher and increasing Y concentrations (~4000–20,000 ppm; Fig. 9A). These basic patterns are mirrored by Gd/Yb ratios (Fig. 9A).

Four-hundred and three laser spots were investigated across 22 different monazite grains located in the thin section of DG167 for both age isotope and trace element data. Except for two outliers that yielded Early Cretaceous dates, which may have elevated com-

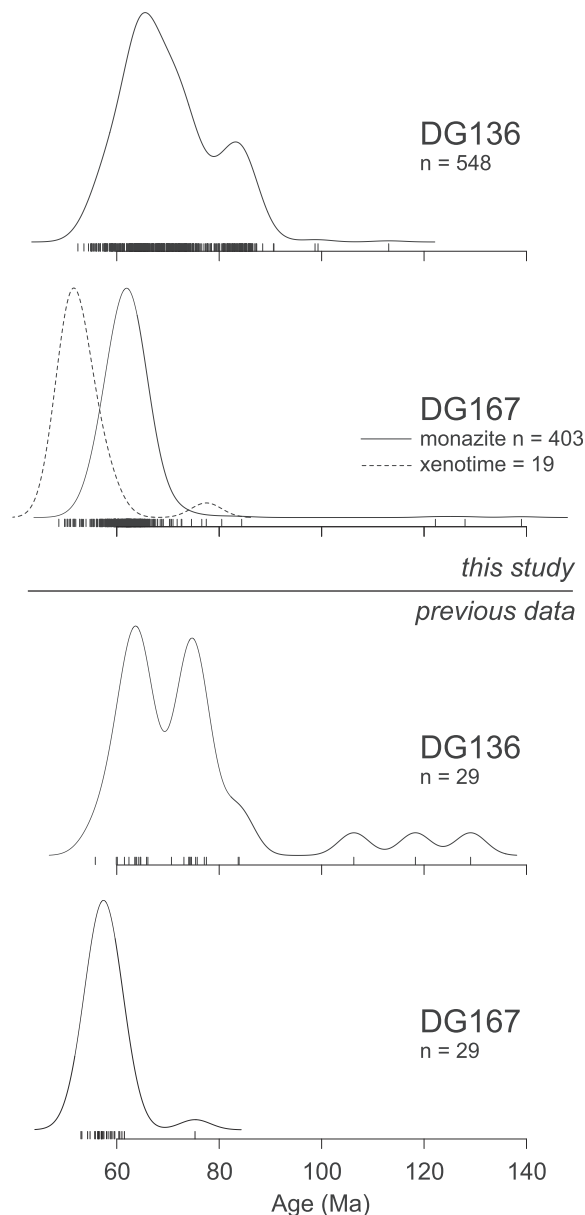


**Fig. 8.** Kernel density estimation plots of the geochronology data reported in the current study versus that previously reported from (Foster et al., 2002, 2004). Vertical axis is normalized density; bandwidth = 3 Ma.

mon Pb, the  $^{208}\text{Pb}/^{232}\text{Th}$  dates range from  $84.4 \pm 2.3$  Ma to  $52.8 \pm 1.2$  Ma (Fig. 10). When plotted as a KDE, the monazite analyses from DG167 define a single peak at ~62 Ma (Fig. 8). Monazite trace element data outline moderate Y concentrations (5000–6000 ppm) at ~65 Ma, but then bifurcate into two populations with younger ages (65–55 Ma). One population is associated with decreasing Y concentrations (4000–5000 ppm) while the other is associated with increasing Y concentrations (6000–20,000 ppm; Fig. 9B). These patterns are mirrored by Gd/Yb ratios, which diverge after ~65 Ma into two younger populations (Fig. 9B). Most of the monazite grains analysed occur in the matrix, typically in association with quartz and biotite. One monazite grain occurred with biotite in, but not enclosed by, a garnet grain (M10), while another (M33) occurred as an inclusion in a different garnet grain (see Supplementary Materials). Neither inclusion, however, is interpreted to have been armoured by garnet. Monazite M10 is in full contact with the matrix, while M33 is intersected by cracks that extend

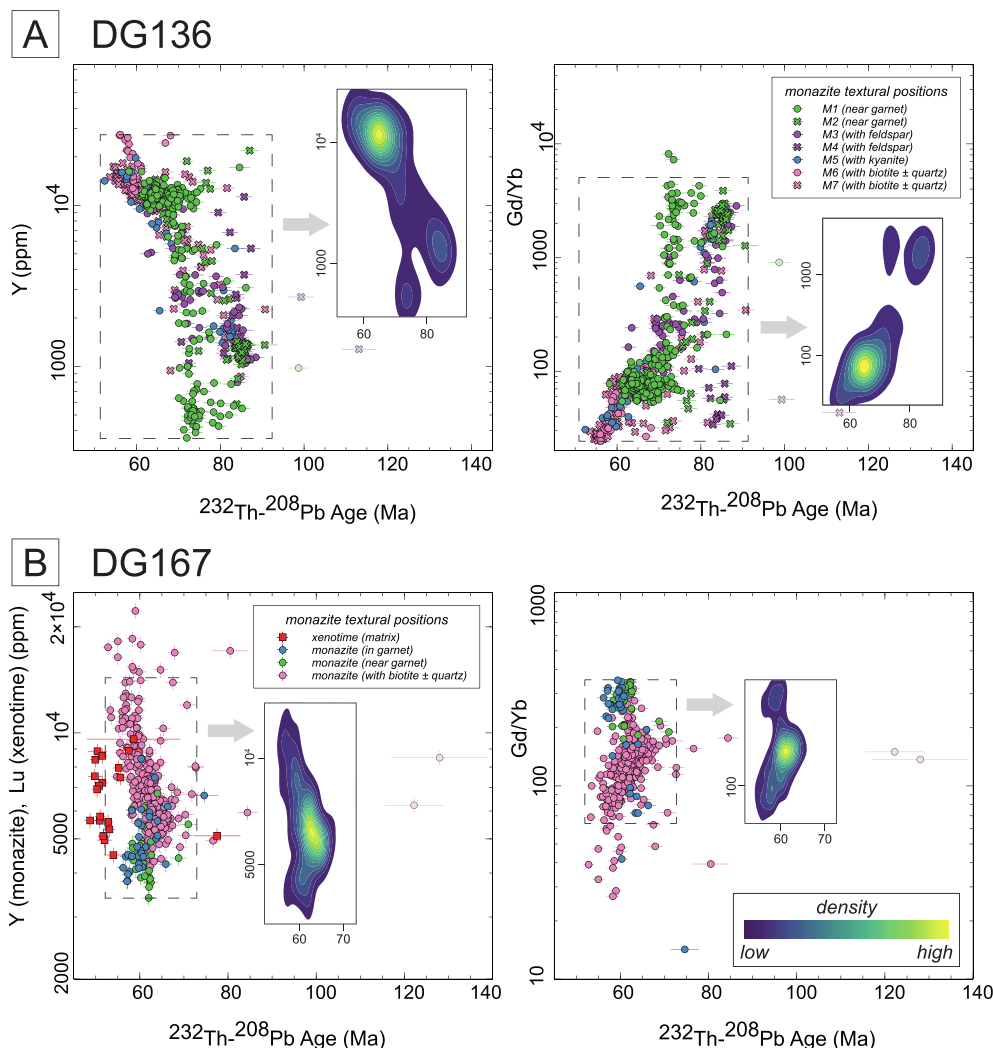


**Fig. 9.** Y vs.  $^{208}\text{Pb}/^{232}\text{Th}$  age and Gd/Yb vs.  $^{208}\text{Pb}/^{232}\text{Th}$  age plots for DG136 (A) and DG167 (B). Plots created using the free software package Veusz (<https://veusz.github.io/>). 2D kernel density estimation plots are also included for greater clarity. Analyses are coloured by textural position, as marked. See text for discussion. Greyed-out data points are not considered robust as they display evidence of elevated common Pb.

across the entire garnet grain (see monazite locations in the [Supplementary Materials](#)). These monazite grains do not show a strong correlation between age and textural position; the dates extracted from the inclusions overlap with the overall peaks mentioned above (Fig. 9B). There is, however, a relationship between textural position and trace element content (Fig. 9B), which is addressed in the Discussion section.

Xenotime was also analysed in DG167 with 21 laser spots across three grains. All xenotime grains were located in the matrix in association with biotite and locally quartz. Isotopic data provide  $^{207}\text{Pb}$ -corrected (Stacey and Kramers, 1975)  $^{206}\text{Pb}/^{238}\text{U}$  xenotime dates that range between  $77.5 \pm 5.3$  Ma and  $48.7 \pm 1.3$  Ma, with most analyses < 60 Ma (Fig. 10). The youngest 12 analyses yield a weighted mean age of  $51.0 \pm 0.7$  Ma (MSWD = 1.2). The trace elements measured with the xenotime analyses do not show any specific pattern with age (Figs. 9B, 10).

#### 4.5. Garnet trace elements

Trace element distributions across garnet in DG136 show minor, non-systematic spatial variation. Noted anomalies coincide with significant cracks in grains (Fig. 4). The inner rim portion of the grains analysed is enriched in HREE, flat in MREE and depleted in LREE relative to the outermost rim (near point A in Fig. 4).

There is no apparent systematic variation in REE concentrations across garnet in DG167. HREE (Y, Lu) distributions are patchy, with local areas of higher concentrations (Fig. 4; see [Supplementary Materials](#)). The concentrations of LREE (Ce) and MREE (Gd) are also patchy with local maxima around inclusions (see [Supplementary Materials](#)).

#### 4.6. Garnet geochronology

Lu-Hf isotopic analyses of garnet from DG136 do not define an isochron and are not presented. With respect to Lu-Hf analysis of DG167, one whole rock analysis was excluded due to an extremely high Hf concentration, while one garnet fraction was excluded due to an anomalously high  $^{176}\text{Hf}/^{177}\text{Hf}$  ratio, perhaps reflecting an unresolved isobaric interference in the measurement. The three remaining garnet fractions and one whole rock analysis of DG167 outline an isochron indicating a Lu-Hf age of  $79 \pm 3$  Ma (Fig. 11) derived using a Model 3 regression, which attributes overdispersion to geological scatter (Ludwig, 2003; Vermeesch, 2018). See [Supplementary Materials](#) for the entire Lu-Hf dataset. The garnet fractions are clustered at the upper end of the isochron. The limited spread in Lu/Hf ratios and the large MSWD (12) of the isochron limit interpreting the robustness of the date. The high MSWD associated with the isochron may reflect protracted or even multi-stage garnet growth (Kohn, 2009).

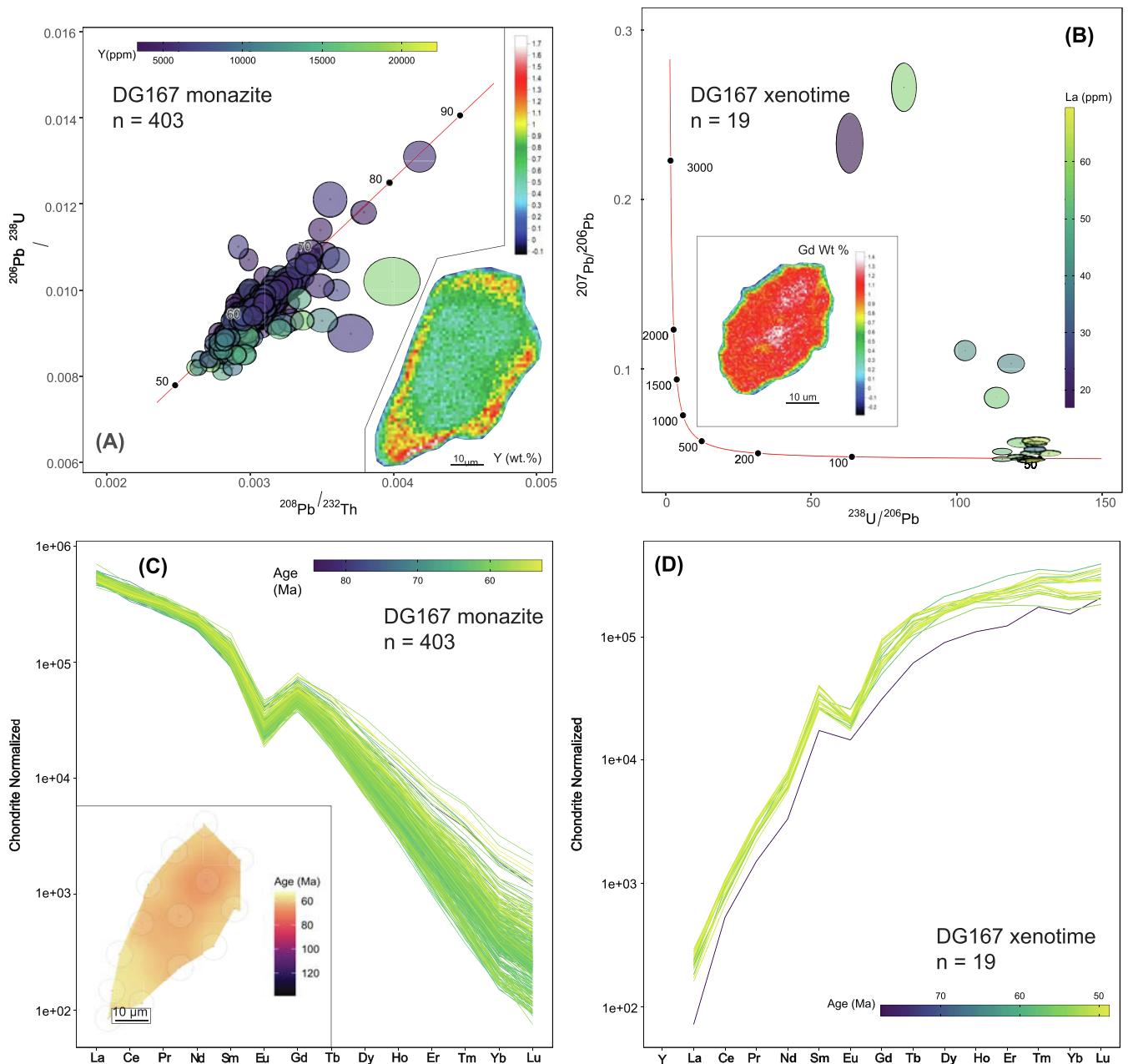


**Fig. 10.** (A) Concordia plots of geochronological data collected in DG167;  $^{208}\text{Pb}/^{232}\text{Th}$  vs.  $^{206}\text{Pb}/^{238}\text{U}$  for monazite, and (B) Tera-Wasserburg  $^{207}\text{Pb}/^{206}\text{Pb}$  vs.  $^{238}\text{U}/^{206}\text{Pb}$  for xenotime. Ellipses are coloured by Y content for monazite and La content for xenotime. Inset in each concordia plot is an example elemental map of a representative grain from the specimen (Y for monazite, Gd for xenotime). Chondrite normalized trace element plot of monazite (C) and xenotime (D) analyses from DG167 coloured by  $^{208}\text{Pb}/^{232}\text{Th}$  age (monazite) and Stacey and Kramers (1975)  $^{207}\text{Pb}$  corrected  $^{206}\text{Pb}/^{238}\text{U}$  age (xenotime). Chondrite values are from McDonough and Sun (1995). Inset in the monazite trace element plot shows an age map of the same grain shown in the concordia plot. All plots were created with the ChrontourR package (Larson, 2020) for the R environment.

Such potential complications are difficult to assess, however, given the general lack of systematic Lu zoning in the garnet. Due to the potential issues with the Lu-Hf date we cautiously interpret it as recording garnet growth ca. 80 Ma.

## 5. Discussion

### 5.1. Monazite behaviour during metamorphism

The P-T paths outlined in the present work follow a similar clockwise shape for both DG136 and DG167, with the path of the

former extending to higher temperature conditions. Those findings are consistent with previous estimates that have outlined higher peak P-T in DG136 (Foster et al., 2004; Gervais and Crowley, 2017).

In the available models for monazite (re)crystallization during metamorphism, its behaviour is strongly influenced by the proportion of melt in the system (Stepanov et al., 2012; Yakymchuk and Brown, 2014; Shrestha et al., 2019), while the fertility of a pelitic protolith to produce melt is strongly influenced by the hydration of the system (White and Powell, 2002). It is common practise to modify the water component of phase equilibria models across the solidus (e.g. Waters, 2019) to better reflect the availability of

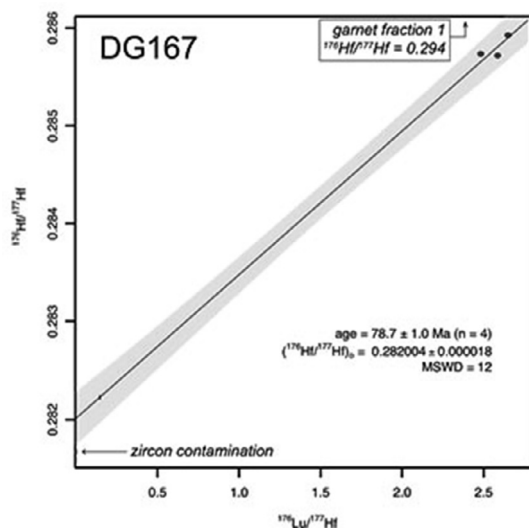


**Fig. 11.** Lu-Hf isochron plot of garnet data from DG167. Diagram generated using IsoplotR (Vermeesch, 2018).

water in the system. This is what we have done in both phase equilibria models developed herein. This approach, however, may not accurately predict the stability of monazite above the solidus. With a saturated solidus, the monazite within specimen DG136 is predicted to completely break down prior to obtaining peak P-T conditions (Fig. 5). Previous studies have suggested metamorphic peak occurred after 70 Ma (Foster et al., 2004; Gervais and Crowley, 2017), yet abundant older monazite remains (Figs. 7, 9A). This difference between observation and prediction may reflect limitations in the ability of the model to reproduce real-world observations or, perhaps, that our model inputs are too simplified.

As a specimen moves beyond the solidus, water contained in hydrous phases consumed by melting reactions will no longer be freed as a fluid phase but will rather be dissolved into the growing melt fraction, progressively dehydrating the residuum. If the melt produced is segregated from the system, perhaps as leucosomes, it will effectively decrease available water. Moreover, past peak conditions, as the melt solidifies, dehydration melting water remains dissolved and becomes concentrated in the decreasing melt fraction. At the solidus, the final melt fraction releases the fluid, which may or may not react with the residuum assemblage. Consequently, the modal proportions of micas predicted by phase equilibria models with water-saturated solidus content are almost always overestimated when compared to actual observed proportions, including in our study, indicating a proportion of water is lost as a free fluid phase once the solidus is crossed on the retrograde path. In such cases, the phase equilibria models generated for a saturated solidus are no longer valid.

To better understand the potential effects of the removal of water from the system we calculated a phase equilibria model with the amount of water calculated from the inferred mineral assemblage (4.08 mol.% H<sub>2</sub>O based on mica mol.% and chemistry) as specimen DG136 crossed over the solidus on the retrograde path (Fig. 12). One of the critical effects of dehydration, even if it is only local, is to stabilize monazite. Using the calculated water content, monazite-bearing assemblages are extended into minimum peak P-T conditions recorded by DG136, consistent with the protracted monazite record in that specimen. While the sharp, irregular zonation in both monazite elemental and age maps in DG136 are consistent with loss of material (Fig. 7), local dehydration, in some form, may provide a mechanism by which to preserve prograde monazite at much higher P-T conditions, or greater total melt vol.% production, than otherwise expected.

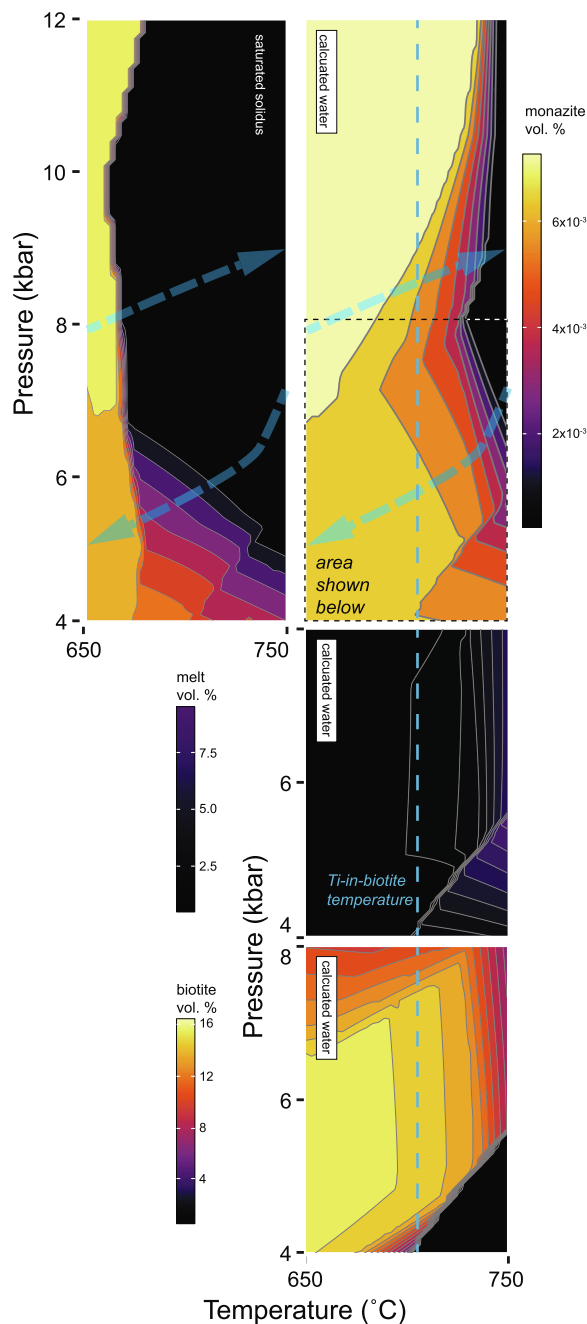


**Fig. 12.** Modal proportions of monazite, melt and biotite for DG136 as modelled based on a saturated solidus or calculated water. See text for discussion. Semi-transparent dashed blue arrows indicate interpreted P-T path. Diagrams created using PixelMap data (de Capitani and Petrakakis, 2010) with the PixelMapR package (Larson and Ambrose, 2021) for the R environment.

## 5.2. Comparison with previous work

The results of monazite geochronology from specimens DG136 and 167 were previously reported in the works of Foster et al. (2002, 2004). Unfortunately, direct comparison of these data with those reported in the current study is complicated by several factors. Firstly, the methods used by Foster et al. (2002, 2004) differ significantly from that outlined herein including both ID-TIMS data and raster-based LA ICP-MS. Moreover, the age systems reported vary not only between methods, but also between specimens. For example, ID-TIMS dates from DG136 and DG167 are reported for the <sup>207</sup>Pb/<sup>235</sup>U and <sup>206</sup>Pb/<sup>238</sup>U systems (Foster et al., 2002), while

LA ICP-MS dates in the same study are reported for the  $^{208}\text{Pb}/^{232}\text{Th}$  system for DG136 and the  $^{207}\text{Pb}/^{235}\text{U}$  and  $^{206}\text{Pb}/^{238}\text{U}$  systems for DG167. The additional dates for DG136 and DG167 from Foster et al. (2004) only include the  $^{207}\text{Pb}/^{235}\text{U}$  and  $^{206}\text{Pb}/^{238}\text{U}$  systems.

Further complicating direct comparison is that the ratios reported for the ID-TIMS dates (Foster et al., 2002) and the LA-MC-ICP-MS dates of DG136 and 167 (Foster et al., 2004) and DG167 (Foster et al., 2002) are corrected for common Pb whereas, in the present study, they are not. Finally, the late Mesozoic to early Paleogene ages of the monazite analysed present significant problems when relying on their U-Pb system. The  $^{206}\text{Pb}/^{238}\text{U}$  system can be affected by excess  $^{206}\text{Pb}$  from the decay of unsupported  $^{230}\text{Th}$  (Schärer, 1984), while the low abundance and slow decay of  $^{235}\text{U}$  to  $^{207}\text{Pb}$  inhibits precise age measurements in that system with typical reported uncertainties of  $\sim \pm 5\text{--}15$  Ma for a  $\sim 60$  Ma date (Foster et al., 2002, 2004).

With the caveats noted above, we will discuss the previously published data only in general terms. Fig. 8 shows KDE plots of previously published dates (using the  $^{208}\text{Pb}/^{232}\text{Th}$  and  $^{207}\text{Pb}/^{235}\text{U}$  systems) and the new data presented here.

Foster et al. (2004) identify monazite having 3 'zones' in DG136. Their 'zone 1' ( $\sim 77\text{--}74$  Ma) monazite grains occur as inclusion in garnet. They are low in Y and are interpreted to have grown during prograde metamorphism. Monazite inclusions within kyanite are the only grains to contain 'zone 2' ( $\sim 65\text{--}60$  Ma) domains, interpreted to have grown with kyanite prior to garnet breakdown. Finally their 'Zone 3' monazite (60–59 Ma) are characterized by relatively high Y content, interpreted to have grown during garnet breakdown and in equilibrium with xenotime (Foster et al., 2004). All monazite analysed in DG136 in the present study were located within the matrix; no inclusions were observed or analyzed. Early monazite growth at ca. 85–80 Ma generally has moderate Y values (Fig. 9A) and moderate to steep negative HREE slopes (Fig. 7) consistent with growth with stable garnet, likely along the prograde path. The grains that yield these ages are dominated by those with a spatial association with feldspar, kyanite, and garnet. A second pulse of monazite growth occurs ca. 75–70 Ma (zone 1 of Foster et al., 2004), associated with low Y concentrations and even steeper HREE slopes (Figs. 7, 9A), perhaps indicating further garnet growth. This population is dominated by monazite near garnet. The  $<70$  Ma monazite analyses (overlapping zones 2 and 3 of Foster et al., 2004) record increasing Y with younger ages (Fig. 9A) and significantly flatter HREE slopes (Fig. 7). These characteristics are interpreted to indicate growth during garnet breakdown along the retrograde portion of the melt-present P-T path. This population includes monazite spatially associated with biotite, quartz, and garnet, consistent with the interpreted P-T path that predicts monazite and biotite growth as the rock crosses the solidus along the retrograde portion (Fig. 12) and that garnet is contributing HREE; Ti-in-biotite temperatures for matrix grains closely match the location of the solidus (Fig. 12). In contrast to the interpretations of Foster et al. (2004) we do not interpret the youngest monazite to have grown in equilibrium with xenotime. There is minimal xenotime in the specimen (none large enough to date) and phase modelling predicts it is likely not stable until significantly lower P-T conditions, after most of the monazite has grown (see Supplementary Materials).

In addition to the previously published monazite dates, Gervais and Crowley (2017) presented 97 new zircon dates on 79 grains from a sample collected from the same unit as DG136. They argue for prograde zircon growth between 77 Ma and 72 Ma (moderate positive HREE slope in zircon) and near-peak supra-solidus P-T growth at  $68.7 \pm 0.9$  Ma (negative HREE slope in zircon) before retrograde growth ca. 65 Ma (positive HREE slope in zircon). The zircon record is broadly consistent with the monazite record outlined herein with the exception of earlier prograde monazite growth

between 90 Ma and 80 Ma. Another potential difference between the monazite and zircon records is the ubiquitous presence of a negative Eu anomaly in monazite analysed herein compared with the virtual absence of such anomaly for the large majority of zircon analyses reported in Gervais and Crowley (2017). This difference may indicate variable growth histories that may not be resolvable with the current data or, alternatively, differential partitioning of Eu into the two minerals (Holder et al., 2020). The expanded history recorded in monazite over zircon exemplifies the proclivity of monazite for sub-solidus zircon during prograde metamorphism, a characteristic that has led to it becoming the mineral of choice for P-T-t path determinations (e.g. Larson et al., 2013; Staples et al., 2013; Ambrose et al., 2015; Mottram et al., 2015; Hacker et al., 2019; Shrestha et al., 2020).

Previous interpretations of the monazite growth history in DG167 by Foster et al. (2004) included growth of 'zone 1' monazite during prograde metamorphism while garnet was stable resulting in relatively low-Y content from  $\sim 60$  Ma to  $\sim 55$  Ma. Subsequent 'zone 2' monazite was interpreted to have grown either along the retrograde path (during garnet breakdown) or at equilibrium with garnet at high temperature at  $\sim 53$  Ma. The P-T-t paths determined herein are consistent with low-Y growth of monazite ca. 68–63 Ma (Fig. 9B), either along the prograde path or at peak P-T. The  $\sim 80$  Ma garnet Lu-Hf age from this sample is compatible with early garnet growth preceding the bulk of monazite crystallization; this is also supported by the occurrence of allanite in garnet cores (Foster et al., 2004). The chemistry of the younger 63–53 Ma monazite population (overlapping zones 1 and 2 of Foster et al., 2004), which has higher Y concentrations, is interpreted to reflect growth along the retrograde path during garnet breakdown. This interpretation is consistent with the spatial association of monazite and biotite and the interpreted P-T path, which predicts concomitant monazite and biotite growth as garnet destabilizes (Fig. 13). It is also consistent with the Ti-in-biotite temperature estimated for matrix biotite grains, which closely coincides with the solidus (Fig. 13). The bifurcation of the Y content in the younger monazite (Fig. 9B) is interpreted to reflect local buffering of REE availability by apatite. The analyses that define those young, low Y populations are from grains spatially associated with garnet. In DG167, there is a high concentration of apatite near garnet (see Supplementary Materials), which may have sequestered, or competed with monazite for REE. The  $\sim 55\text{--}49$  Ma xenotime dates measured in DG167 are interpreted to reflect (re)crystallization dominantly after monazite along the retrograde path.

### 5.3. REE partitioning

While the present study outlines critical observations about potential complications for understanding REE partitioning between monazite and garnet (i.e. the potential effect of tertiary phases) the specimens are not conducive to a robust analysis of this phenomena. For example, there are few monazite inclusions within garnet to provide textural information and those that do occur are not armoured (see above). Moreover, garnet in both specimens is not systematically zoned, making linkages between matrix monazite and specific chemical zones tenuous at best. Building on the existing research into monazite/garnet REE partitioning (e.g. Buick et al., 2006; Hermann and Rubatto, 2003; Rubatto et al., 2006; Warren et al., 2018; Hacker et al., 2019) may benefit from the monazite grain mapping petrochronology approach applied herein, but requires specimens with the appropriate textural and mineral zoning characteristics to be able to meaningfully assess potential equilibrium pairs. It is possible that emerging analytical methods, such as *in situ* Lu-Hf geochronology (Simpson et al., 2021), may allow direct time linkages between garnet zones and chronometer zonation. This would help eliminate



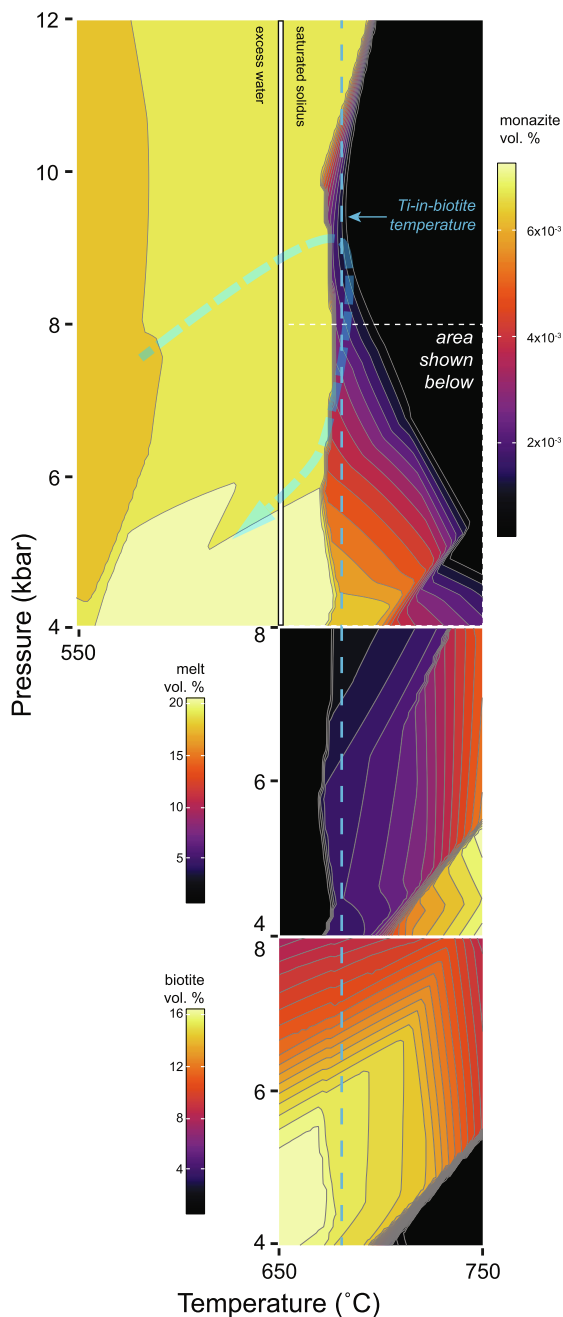


**Fig. 13.** Modal proportions of monazite, melt and biotite for DG167 as modelled based on a water in excess or a saturated solidus. See text for discussion. Semi-transparent dashed blue arrow indicates interpreted P-T path. Diagrams created using PixelMap data (de Capitani and Petrakakis, 2010) with the PixelMapR package (Larson and Ambrose, 2021) for the R environment.

some of the assumptions currently necessary when examining potential equilibrium partitioning between different phases.

## 6. Conclusions

In general, the basic framework that Foster et al. (2000, 2002, 2004), Gibson et al. (2004) and other studies developed to interpret monazite elemental zoning in the context of metamorphic P-T paths appears to be generally robust. With some notable exceptions, the basic observations that link monazite REE contents to garnet stability and monazite stability to anatexis appear to be consistent with observed data. The present work does, however,

demonstrate the advantages of applying modern methodologies to this problem and expanding the number of analyses included in the work. For example, *in situ* investigation of monazite spatially associated with garnet and apatite in this work shows that low Y monazite can be associated with garnet breakdown if buffered locally, whereas the ‘typical’ interpretation of low Y monazite would be that garnet was stable or growing during monazite (re) crystallization. This work further demonstrates the requirement to understand not only the spatial and textural position of monazite, but also all other phases such as garnet, apatite and/or xenotime that may participate in the overall REE budget of a rock.

## Declaration of Competing Interest

The authors declare that they have no known competing financial interests or personal relationships that could have appeared to influence the work reported in this paper.

## Acknowledgements

C. Montomoli is thanked for their assistance in having the coverslips removed from the thin sections. Funding for the project includes an NSERC Discovery Grant and CFI JELF award to K. Larson. Thoughtful, constructive reviews by R. Soucy La Roche, J. Garber and K. Mahan, and editorial handling by Associate Editor Dr. R. Palin improved the manuscript. M. Button is thanked for his analytical expertise. The full dataset related to this study can be freely accessed through the Open Science Framework: doi.org/10.17605/OSF.IO/Z8DJJP.

## Appendix A. Supplementary data

Supplementary data to this article can be found online at <https://doi.org/10.1016/j.gsf.2021.101340>.

## References

- Akima, H., 1978. A method of bivariate interpolation and smooth surface fitting for irregularly distributed data points. *ACM Trans. Math. Softw.* 4 (2), 148–159.
- Aleinikoff, J.N., Schenck, W.S., Plank, M.O., Srogi, L., Fanning, C.M., Kamo, S.L., Bosbyshell, H., 2006. Deciphering igneous and metamorphic events in high-grade rocks of the Wilmington Complex, Delaware: Morphology, cathodoluminescence and backscattered electron zoning, and SHRIMP U-Pb geochronology of zircon and monazite. *Geol. Soc. Am. Bull.* 118 (1-2), 39–64.
- Ambrose, T.K., Larson, K.P., Guilmette, C., Cottle, J.M., Buckingham, H., Rai, S., 2015. Lateral extrusion, underplating, and out-of-sequence thrusting within the Himalayan metamorphic core, Kanchenjunga, Nepal. *Lithosphere* 7 (4), 441–464.
- Brown, R.L., Gibson, H.D., 2006. An argument for channel flow in the southern Canadian Cordillera and comparison with Himalaya tectonics. *Geol. Soc. London Spec. Pub.* 268, 543–559.
- Brown, R.L., Carr, S.D., Johnson, B.J., Coleman, V.J., Cook, F.A., Varsek, J.L., 1992. The Monashee decollement of the southern Canadian Cordillera: a crustal-scale shear zone linking the Rocky Mountain Foreland belt to lower crust beneath accreted terranes. In: McClay, K.R. (Ed.), *Thrust Tectonics*. Springer, Netherlands, Dordrecht, pp. 357–364.
- Buick, I.S., Hermann, J., Williams, I.S., Gibson, R.L., Rubatto, D., 2006. A SHRIMP U-Pb and LA-ICP-MS trace element study of the petrogenesis of garnet–cordierite–orthoamphibole gneisses from the Central Zone of the Limpopo Belt, South Africa. *Lithos* 88, 150–172.
- Cheng, H., King, R.L., Nakamura, E., Vervoort, J.D., Zhou, Z., 2008. Coupled Lu–Hf and Sm–Nd geochronology constrains garnet growth in ultra-high-pressure eclogites from the Dabie orogen. *J. Metamorph. Geol.* 26 (7), 741–758.
- Colpron, M., Nelson, J.L., 2011. A digital atlas of terranes for the northern Cordillera. BC Geofile, 11.
- Connolly, J.A.D., 1990. Multivariable phase diagrams; an algorithm based on generalized thermodynamics. *Am. J. Sci.* 290 (6), 666–718.
- Cottle, J., Lederer, G., Larson, K., 2019. The monazite record of pluton assembly: Mapping manaslu using petrochronology. *Chem. Geol.* 530, 119309.
- de Capitani, C., Brown, T.H., 1987. The computation of chemical equilibrium in complex systems containing non-ideal solutions. *Earth Planet. Sci. Lett.* 51 (10), 2639–2652.

- de Capitani, C., Petrakakis, K., 2010. The computation of equilibrium assemblage diagrams with Theriak/Domino software. *Am. Mineral.* 95 (7), 1006–1016.
- Donovan, J.J., Singer, J.W., Armstrong, J.T., 2016. A new EPMA method for fast trace element analysis in simple matrices. *Am. Mineral.* 101 (8), 1839–1853. <https://doi.org/10.2138/am-2016-5628>.
- Enami, M., Nishiyama, T., Mouri, T., 2007. Laser Raman microspectrometry of metamorphic quartz: A simple method for comparison of metamorphic pressures. *Am. Mineral.* 92 (8–9), 1303–1315.
- Foster, G., Kinny, P., Vance, D., Prince, C., Harris, N., 2000. The significance of monazite U-Th–Pb age data in metamorphic assemblages; a combined study of monazite and garnet chronometry. *Earth Planet. Sci. Lett.* 181 (3), 327–340.
- Foster, G., Gibson, H.D., Parrish, R., Horstwood, M., Fraser, J., Tindle, A., 2002. Textural, chemical and isotopic insights into the nature and behaviour of metamorphic monazite. *Chem. Geol.* 191 (1–3), 183–207.
- Foster, G., Parrish, R.R., Horstwood, M.S.A., Chenery, S., Pyle, J., Gibson, H.D., 2004. The generation of prograde P–T–t points and paths; a textural, compositional, and chronological study of metamorphic monazite. *Earth Planet. Sci. Lett.* 228 (1–2), 125–142.
- Fumes, R.A., Luvizotto, G.L., Moraes, R., Heilbron, M., Vlach, S.R.F., 2019. Metamorphic modeling and petrochronology of metapelitic rocks from Luminárias Nappe, southern Brasília belt (SE Brazil). *Braz. J. Geol.* 49, 1–25.
- Garber, J.M., Hacker, B.R., Kylander-Clark, A.R.C., Stearns, M., Seward, G., 2017. Controls on trace element uptake in metamorphic titanite: implications for petrochronology. *J. Petrol.* 58, 1031–1057.
- Gervais, F., 2018. Three modes of isograd formation in the northern Monashee Complex of the Canadian Cordillera. *Geol. Soc., London, Spec. Publ.* 478 (1), 373–388.
- Gervais, F., Brown, R.L., 2011. Testing modes of exhumation in collisional orogens: Synconvergent channel flow in the southeastern Canadian Cordillera. *Lithosphere* 3, 55–75.
- Gervais, F., Crowley, J.L., 2017. Prograde and near-peak zircon growth in a migmatitic pelitic schist of the southeastern Canadian Cordillera. *Lithos* 282–283, 65–81.
- Gervais, F., Trapay, P.-H., 2021. Testing solution models for phase equilibrium (forward) modeling of partial melting experiments. *Contrib. Mineral. Petrol.* 176, 1–19. <https://doi.org/10.1007/s00410-020-01762-5>.
- Gibson, H.D., 1997. Thermotectonic evolution of the northern Monashee Complex, southern Omineca Belt, southeastern British Columbia. M.S. thesis, Carleton University.
- Gibson, H.D., Brown, R.L., Parrish, R.R., 1999. Deformation-induced inverted metamorphic field gradients: an example from the southeastern Canadian Cordillera. *J. Struct. Geol.* 21 (7), 751–767.
- Gibson, H.D., Carr, S.D., Brown, R.L., Hamilton, M.A., 2004. Correlations between chemical and age domains in monazite, and metamorphic reactions involving major pelitic phases: an integration of ID-TIMS and SHRIMP geochronology with Y-Th–U X-ray mapping. *Chem. Geol.* 211 (3–4), 237–260.
- Gibson, H.D., Brown, R.L., Carr, S.D., 2008. Tectonic evolution of the Selkirk fan, southeastern Canadian Cordillera: A composite Middle Jurassic–Cretaceous orogenic structure. *Tectonics* 27 (6), TC6007.
- Godet, A., Guilmette, C., Labrousse, L., Davis, D.W., Smit, M.A., Cutts, J.A., Vanier, M., Lafrance, I., Charette, B., 2020. Complete metamorphic cycle and long-lived anatexis in the c. 2.1 Ga Mistinibi Complex, Canada. *J. Metamorph. Geol.* 38, 235–264.
- Hacker, B., Kylander-Clark, A., Holder, R., 2019. REE partitioning between monazite and garnet: Implications for petrochronology. *J. Metamorph. Geol.* 37, 227–237.
- Henry, D.J., Guidotti, C.V., Thomson, J.A., 2005. The Ti-saturation surface for low-to-medium pressure metapelitic biotites: Implications for geothermometry and Ti-substitution mechanisms. *Am. Mineral.* 90, 316–328.
- Hermann, J., Rubatto, D., 2003. Relating zircon and monazite domains to garnet growth zones: age and duration of granulite facies metamorphism in the Val Malenco lower crust. *J. Metamorph. Geol.* 21, 833–852.
- Holder, R.M., Yakymchuk, C., Viète, D.R., 2020. Accessory mineral Eu anomalies in suprasolidus rocks: Beyond feldspar. *Geochem. Geophys. Geosyst.* 21 (8), e2020GC009052. <https://doi.org/10.1029/2020GC009052>.
- Holland, T.J.B., Powell, R., 1998. An internally consistent thermodynamic data set for phases of petrological interest. *J. Metamorph. Geol.* 16 (3), 309–343.
- Johnson, T.A., Vervoort, J.D., Ramsey, M.J., Aleinikoff, J.N., Southworth, S., 2018. Constraints on the timing and duration of orogenic events by combined Lu–Hf and Sm–Nd geochronology: an example from the Grenville orogeny. *Earth Planet. Sci. Lett.* 501, 152–164.
- Johnson, T.A., Vervoort, J.D., Ramsey, M.J., Southworth, S., Mulcahy, S.R., 2020. Tectonic evolution of the Grenville Orogen in the central Appalachians. *Precambrian Res.* 346, 105740.
- Johnson, T., Yakymchuk, C., Brown, M., 2021. Crustal melting and suprasolidus phase equilibria: From first principles to the state-of-the-art. *Earth-Sci. Rev.* 221, 103778.
- Kerswell, B., Harvey, K., Kohn, M., 2021. An app to explore 1-D data and perform unsupervised clustering by Gaussian Mixture Modelling. *Peakfit Explorer*. <https://doi.org/10.17605/OSF.IO/2BU3C>.
- Kohn, M.J., 2009. Models of garnet differential geochronology. *Geochim. Cosmochim. Acta* 73 (1), 170–182.
- Kohn, M.J., Spear, F.S., 2000. Retrograde net transfer reaction insurance for pressure-temperature estimates. *Geology* 28, 1127–1130.
- Kohn, M.J., Wieland, M.S., Parkinson, C.D., Upreti, B.N., 2005. Five generations of monazite in Langtang gneisses: implications for chronology of the Himalayan metamorphic core. *J. Metamorph. Geol.* 23 (5), 399–406.
- Kylander-Clark, A.R.C., Hacker, B.R., Cottle, J.M., 2013. Laser-ablation split-stream ICP petrochronology. *Chem. Geol.* 345, 99–112.
- Larson, K.P., Ambrose, T., 2021. Scripts written in R that allow plotting/visualization of the PIXMAP data output from Theriak-Domino. *PixelMapR*. <https://doi.org/10.17605/OSF.IO/ZD849>.
- Larson, K.P., Gervais, F., Kellett, D.A., 2013. A P–T–t discontinuity in east-central Nepal: Implications for the evolution of the Himalayan mid-crust. *Lithos* 179, 275–292.
- Larson, K.P., Ali, A., Shrestha, S., Soret, M., Cottle, J.M., Ahmad, R., 2019. Timing of metamorphism and deformation in the Swat valley, northern Pakistan: Insight into garnet-monzite HREE partitioning. *Geosci. Front.* 10 (3), 849–861.
- Larson, K.P., 2020. Scripts for plotting geochronology and petrochronology data in R. *ChrontourR*. <https://doi.org/10.17605/OSF.IO/P46MB>.
- Ludwig, K.R., 2003. *Isoplot 3.00*. Berkeley Geochronology Center Special Publication 4.
- McDonough, W.F., Sun, S.-s., 1995. The Composition of the Earth. *Chem. Geol.* 120 (3–4), 223–253.
- McFarlane, C.R.M., Connelly, J.N., Carlson, W.D., 2005. Monazite and xenotime petrogenesis in the contact aureole of the Makhavinekh Lake Pluton, northern Labrador. *Contrib. Mineral. Petrol.* 148 (5), 524–541.
- McKinney, S.T., Cottle, J.M., Lederer, G.W., 2015. Evaluating rare earth element (REE) mineralization mechanisms in Proterozoic gneiss, Music Valley, California. *Geol. Soc. Am. Bull.* 127 (7–8), 1135–1152.
- Mottram, C.M., Parrish, R.R., Regis, D., Warren, C.J., Argles, T.W., Harris, N.B.W., Roberts, N.M.W., 2015. Using U–Th–Pb petrochronology to determine rates of ductile thrusting: Time windows into the Main Central Thrust, Sikkim Himalaya. *Tectonics* 34 (7), 1355–1374.
- Paton, C., Woodhead, J.D., Hellstrom, J.C., Hergt, J.M., Greig, A., Maas, R., 2010. Improved laser ablation U–Pb zircon geochronology through robust downhole fractionation correction. *Geochem. Geophys. Geosyst.* 11 (3), Q0AA06.
- Paton, C., Hellstrom, J., Paul, B., Woodhead, J., Hergt, J., 2011. Iolite: Freeware for the visualisation and processing of mass spectrometric data. *J. Anal. At. Spectrom.* 26 (12), 2508–2518.
- Powell, R., Holland, T., Worley, B., 1998. Calculating phase diagrams involving solid solutions via non-linear equations, with examples using THERMOCALC. *J. Metamorph. Geol.* 16 (4), 577–588.
- Pyle, J.M., Spear, F.S., Rudnick, R.L., McDonough, W.F., 2001. Monazite-xenotime-garnet equilibrium in metapelites and a new monazite-garnet thermometer. *J. Petrol.* 42, 2083–2107.
- Read, P.B., Brown, R.L., 1981. Columbia River fault zone: southeastern margin of the Shuswap and Monashee complexes, southern British Columbia. *Can. J. Earth Sci.* 18 (7), 1127–1145.
- Rubatto, D., Hermann, J., Buick, I.S., 2006. Temperature and bulk composition control on the growth of monazite and zircon during low-pressure anatexis (Mount Stafford, Central Australia). *J. Petrol.* 47, 1973–1996.
- Scammell, R.J., Brown, R.L., 1990. Cover gneisses of the Monashee Terrane: a record of synsedimentary rifting in the North American Cordillera. *Can. J. Earth Sci.* 27 (5), 712–726.
- Schärer, U., 1984. The effect of initial <sup>230</sup>Th disequilibrium on young U–Pb ages: the Makalu case, Himalaya. *Earth Planet. Sci. Lett.* 67 (2), 191–204.
- Shrestha, S., Larson, K.P., Martin, A.J., Guilmette, C., Smit, M.A., Cottle, J.M., 2020. The greater Himalayan thrust belt: Insight into the assembly of the exhumed Himalayan metamorphic core, Modi khola valley, central Nepal. *Tectonics* 39, e2020TC006252. <https://doi.org/10.1029/2020tc006252>.
- Shrestha, S., Larson, K.P., Dueterhoef, E., Soret, M., Cottle, J.M., 2019. Thermodynamic modelling of phosphate minerals and its implications for the development of P–T–t histories: A case study in garnet – monazite bearing metapelites. *Lithos* 334–335, 141–160.
- Simony, P.S., Carr, S.D., 2011. Cretaceous to Eocene evolution of the southeastern Canadian Cordillera: Continuity of Rocky Mountain thrust systems with zones of “in-sequence” mid-crustal flow. *J. Struct. Geol.* 33 (9), 1417–1434.
- Simpson, A., Gilbert, S., Tamlyn, R., Hand, M., Spandler, C., Gillespie, J., Nixon, A., Glorie, S., 2021. In-situ Lu–Hf geochronology of garnet, apatite and xenotime by LA ICP MS/MS. *Chem. Geol.* 577, 120299.
- Spear, F.S., Pyle, J.M., 2002. Apatite, Monazite, and Xenotime in Metamorphic Rocks. *Rev. Mineral. Geochem.* 48 (1), 293–335.
- Spear, F.S., Pyle, J.M., 2010. Theoretical modeling of monazite growth in a low-Ca metapelite. *Chem. Geol.* 273 (1–2), 111–119.
- Stacey, J.S., Kramers, J.D., 1975. Approximation of terrestrial lead isotope evolution by a two-stage model. *Earth Planet. Sci. Lett.* 26 (2), 207–221.
- Staples, R.D., Gibson, H.D., Berman, R.G., Ryan, J.J., Colpron, M., 2013. A window into the Early to mid-Cretaceous infrastructure of the Yukon-Tanana terrane recorded in multi-stage garnet of west-central Yukon, Canada. *J. Metamorph. Geol.* 31 (7), 729–753.
- Stearns, M.A., Hacker, B.R., Ratschbacher, L., Lee, J., Cottle, J.M., Kylander-Clark, A., 2013. Synchronous Oligocene–Miocene metamorphism of the Pamir and the north Himalaya driven by plate-scale dynamics. *Geology* 41 (10), 1071–1074.
- Stepanov, A.S., Hermann, J., Rubatto, D., Rapp, R.P., 2012. Experimental study of monazite/melt partitioning with implications for the REE, Th and U geochemistry of crustal rocks. *Chem. Geol.* 300–301, 200–220.
- Tomascak, P.B., Krogstad, E.J., Walker, R.J., 1996. U–Pb Monazite Geochronology of Granitic Rocks from Maine: Implications for Late Paleozoic Tectonics in the Northern Appalachians. *J. Geol.* 104 (2), 185–195.
- Vermesch, P., 2018. IsoplotR: A free and open toolbox for geochronology. *Geosci. Front.* 9 (5), 1479–1493.

- Warren, C.J., Greenwood, L.V., Argles, T.W., Roberts, N.M.W., Parrish, R.R., Harris, N. B.W., 2018. Garnet–monazite rare earth element relationships in sub-solidus metapelites: a case study from Bhutan. *Geol. Soc., Lond., Spec. Publ.* 478 (1), 145–166.
- Waters, D.J., 2019. Metamorphic constraints on the tectonic evolution of the High Himalaya in Nepal: the art of the possible. *Geol. Soc., Lond., Spec. Publ.* 483, SP483-2018–187.
- Wheeler, J.O., McFeely, P., Canada, G.S., 1991. Tectonic assemblage map of the Canadian Cordillera and adjacent parts of the United States of America: Map 1712A.
- White, R.W., Powell, R., 2002. Melt loss and the preservation of granulite facies mineral assemblages. *J. Metamorph. Geol.* 20, 621–632.
- White, R.W., Powell, R., Holland, T.J.B., 2007. Progress relating to calculation of partial melting equilibria for metapelites. *J. Metamorph. Geol.* 25, 511–527.
- Whitney, D.L., Evans, B.W., 2010. Abbreviations for names of rock-forming minerals. *Am. Mineral.* 95, 185–187.
- Williams, M.L., Jercinovic, M.J., Mahan, K.H., Dumond, G., 2017. Electron microprobe petrochronology. *Rev. Mineral. Geochem.* 83, 153–182.
- Woodsworth, G.J., 1977. Homogenization of Zoned Garnets From Pelitic Schists. *Can. Mineral.* 15, 230–242.
- Yakymchuk, C., Brown, M., 2014. Behaviour of zircon and monazite during crustal melting. *J. Geol. Soc. London* 171, 465–479.